OXFORD

Journal of Petrology, 2025, **66**, egaf036
https://doi.org/10.1093/petrology/egaf036
ADVANCE ACCESS PUBLICATION DATE 01 MAY 2025
Original Manuscript

Formation of Spongy Clinopyroxene: Insights from Eclogitic Inclusions in Diamonds

WENYU WANG[1,2,*], NESTER M. KOROLEV[2,3], EKATERINA S. KISEEVA[2,3,*], RONDI M. DAVIES[3,4], YAAKOV WEISS[5], MAYA KOPYLOVA[6], W. HENRY TOWBIN[7], FANG HUANG[1,8], ANDY E. MOORE[9] and EVGENIY A. VASILEV[10]

[1]State Key Laboratory of Lithospheric and Environmental Coevolution, School of Earth and Space Sciences, University of Science and Technology of China, No. 96 Jinzhai Road, Baohe District, Hefei 230026, Anhui, China
[2]School of Biological, Earth and Environmental Sciences, University College Cork, Distillery Fields, North Mall, Cork T23 N73K, Ireland
[3]Department of Earth and Planetary sciences, American Museum of Natural History, 200 Central Park West, New York, NY 10024, USA
[4]Department of Biological Sciences and Geology, Queensborough Community College, City University of New York, 56th Avenue, Bayside, NY 11364, USA
[5]The Freddy and Nadine Herrmann Institute of Earth Sciences, The Edmond J. Safra Campus - Givat Ram, Hebrew University of Jerusalem, Jerusalem 91904, Israel
[6]Department of Earth, Ocean and Atmospheric Sciences, The University of British Columbia, 2207 Main Mall, Vancouver, BC V6T 1Z4, Canada
[7]Gemmological Institute of America, 50 W. 47th Street, New York 10036, NY, USA
[8]CAS Center for Excellence in Comparative Planetology, University of Science and Technology of China, No. 96 Jinzhai Road, Baohe District, Hefei 230026, China
[9]Department of Geology, Rhodes University, Artillery Road, Grahamstown 6140, South Africa
[10]Department of Mineralogy, Crystallography and Petrography, Saint-Petersburg Mining University, 2, 21st Line V.O., Saint-Petersburg 199106, Russia
*Corresponding authors: Wenyu Wang: State Key Laboratory of Lithospheric and Environmental Coevolution, School of Earth and Space Sciences, University of Science and Technology of China, No. 96 Jinzhai Road, Baohe District, Hefei 230026, Anhui, China, Telephone: +353 21 490 3000, E-mail: wwyustc@mail.ustc.edu.cn; Ekaterina S. Kiseeva: American Museum of Natural History, Department of Earth and Planetary Sciences, 200 Central Park West, New York, NY 10024, USA, Telephone: +1 (212) 769-5401, E-mail: kkiseeva@amnh.org

Spongy clinopyroxene is common in most mantle-derived xenoliths and megacrysts of eclogitic and peridotitic parageneses. Its formation is commonly attributed to the partial melting of a primary clinopyroxene in response to various factors, including changes in pressure and temperature or infiltration of external melts or fluids. In order to study the mechanism of spongy clinopyroxene formation in detail, we selected six eclogitic clinopyroxene inclusions in diamonds with varying amounts of spongy clinopyroxene (from ~10 to 100%). We employed computed tomography, electron microprobe analysis, and Raman spectroscopy to study the textural characteristics, major element concentrations, and the types of volatiles present in both phases. We also used pMELTS to model the compositions of spongy clinopyroxene and associated melts produced by the melting of primary clinopyroxene over a range of pressures and temperatures. We compare these results with estimates from major element thermobarometry of the spongy clinopyroxene. We conclude that the studied spongy clinopyroxene is the solid product of partial melting that occurs upon decompression of the primary clinopyroxene within the diamond in a near-closed system. Melting of the primary clinopyroxene occurred continuously or in pulses at different depths during the diamond's ascent to Earth's surface and produced variable spongy clinopyroxene and melt compositions even within the same inclusion. This is possible due to relatively rapid kimberlite ascent. The degrees of melting are various and unexpectedly high for mantle melting (between <10 and 60% with an average of ~20–30%). The produced melts are highly silicic, phonolitic, and alkali-rich. pMELTS modelling shows the spongy clinopyroxene compositions can be reproduced at pressures between 0.5–2.7 GPa and temperatures of 850–1300°C, with the majority of them satisfying the P–T conditions of 1–2 GPa and 1100–1300°C. This indicates decompression melting of primary clinopyroxene at shallow upper mantle or lower crustal conditions.

Key words: diamond inclusions; kimberlite ascent; spongy clinopyroxene; thermobarometry

INTRODUCTION

Spongy (or cracking, or crinkled) clinopyroxene is a common secondary mineral in eclogitic and peridotitic mantle xenoliths and megacrysts (Taylor & Neal, 1989; Misra *et al.*, 2004; Ma *et al.*, 2015; Pan *et al.*, 2018; Lebedeva *et al.*, 2022; Chien *et al.*, 2024; Wang *et al.*, 2024). The formation of secondary spongy clinopyroxene has been reported in xenoliths of eclogitic affinity across multiple cratons: Arkhangelsk province (Lebedeva *et al.*, 2022); Kaapvaal Craton: Bellsbank (Taylor & Neal, 1989), Bobbejaan (Caporuscio & Smyth, 1990), Jagersfontein (Pyle & Haggerty, 1998), and Roberts Victor (Windom & Boettcher, 1980; Kiseeva *et al.*, 2017); Kasai Craton (Korolev *et al.*, 2021); North Atlantic Craton (Pobric *et al.*, 2020); Slave Craton (De Stefano *et al.*, 2009); Sask Craton (Czas *et al.*, 2018); Siberian Craton (Spetsius & Taylor, 2002): Mir (Beard *et al.*, 1996) and Udachnaya (Sobolev *et al.*, 1999; Misra *et al.*, 2004); West African craton: Koidu kimberlites (Fung & Haggerty, 1995; Barth *et al.*, 2002), and many other locations.

Texturally, spongy clinopyroxene is typically concentrated at the rims of the primary clinopyroxene, or along veins and fractures inside of it (Taylor & Neal, 1989; Misra *et al.*, 2004; Kargin *et al.*, 2017; Pan *et al.*, 2018). The spongy texture typically presents as a series of interconnected pores or melt pools that form a network, characterised by irregular shapes and varying degrees of porosity or melt pool abundance. Pores develop as a result of the

RECEIVED AUGUST 19, 2024; **REVISED** APRIL 10, 2025; **ACCEPTED** APRIL 13, 2025

rapid escape of melt. In case the melt has not been drained off, spongy clinopyroxene is frequently accompanied or intergrown with an alkali-rich phase, which differs between xenoliths and can be either a feldspar (albitic plagioclase or K-feldspar) and/or glass. It has also been observed in association with micro-spinel (Spetsius & Taylor, 2002).

The compositions of spongy clinopyroxene of eclogitic paragenesis are always more refractory, with a diopsidic composition in comparison with the primary omphacite (Misra *et al.*, 2004; Taylor & Anand, 2004). This is usually attributed to its formation at lower pressures than the primary omphacitic clinopyroxene, consistent with decreasing partitioning of Na into clinopyroxene at lower pressure (Blundy *et al.*, 1995). Due to their initial low-Na content, a more refractory, lower-Na composition of spongy clinopyroxene is less pronounced in peridotitic pyroxenes (Kopylova *et al.*, 2019).

There is little agreement regarding the temperatures and pressures in which spongy clinopyroxene can form, as well as the proportion of externally introduced melt or fluid that aid in its formation. Proposed mechanisms for the formation of spongy clinopyroxene greatly differ based on the mantle-derived rock type and the extent of interaction with the host kimberlitic fluid or magma: eclogites (Spetsius & Taylor, 2002; Misra *et al.*, 2004; Lebedeva *et al.*, 2022), peridotites (*e.g.*, Su *et al.*, 2011; Lu *et al.*, 2015; Pan *et al.*, 2018), and clinopyroxene megacrysts (Bussweiler *et al.*, 2016; Kargin *et al.*, 2017; Abersteiner *et al.*, 2019).

Nevertheless, it is commonly agreed that spongy textures form as a result of partial melting; however, the main trigger of this melting is still a matter of debate (Su *et al.*, 2011; Lu *et al.*, 2015; Ma *et al.*, 2015; Pan *et al.*, 2018).

The main unresolved controversies regarding the origin of spongy clinopyroxene are: (1) the pressure–temperature (P–T) conditions of its formation, reflecting whether this occurred in the lithospheric mantle (for peridotites: 1.0–2.7 GPa (Carpenter *et al.*, 2002; Table 1 in Chien *et al.*, 2024; Ionov *et al.*, 1994; Lu *et al.*, 2015; Schiano & Clocchiatti, 1994; Schiano *et al.*, 1994); for eclogites: 3–6 GPa (Misra *et al.*, 2004; Lebedeva *et al.*, 2022); for clinopyroxene megacrysts: <2.5 GPa (Bussweiler *et al.*, 2016) or lower crust (for peridotites: <1 GPa (Ma *et al.*, 2015; Pan *et al.*, 2018); for eclogites: <1.5 GPa (Spetsius & Taylor, 2002; Taylor & Anand, 2004); (2) the mechanism of partial melting of primary clinopyroxene, which can include induced melting as a result of interaction with metasomatic melts/fluids (Griffin *et al.*, 1984; Menzies *et al.*, 1985), kimberlitic–carbonatitic melts/fluids (Spetsius & Taylor, 2002; Huang *et al.*, 2012; Huang *et al.*, 2014; Abersteiner *et al.*, 2019), or incipient melting; for example, decompression melting (Su *et al.*, 2011; Kiseeva *et al.*, 2017).

Unravelling the mechanism of spongy clinopyroxene formation in mantle xenoliths is hampered by an extensive surface or near-surface modification of the samples, which usually results in the crystallisation of low-pressure secondary phases such as calcite, zeolites, barite, and others. Low-pressure alteration can also cause compositional modification of alkali-rich melt pockets associated with spongy clinopyroxene (Misra *et al.*, 2004; Kiseeva *et al.*, 2017).

One way to address this problem is through studies of mineral inclusions in diamonds. Although very rare, there are a small number of studies that report the presence of primary and spongy clinopyroxene in inclusions in diamonds (Taylor *et al.*, 2000; Liu *et al.*, 2009; Sobolev *et al.*, 2009). Among these, Taylor *et al.* (2000) conducted a detailed chemical characterisation of primary and spongy clinopyroxenes within the same inclusion. Although all reported inclusions are found in three diamonds from a single Udachnaya (Siberia) eclogitic xenolith, the major and trace element compositions of the inclusions span almost two-thirds of the range of clinopyroxenes found in all xenoliths from the Udachnaya kimberlite (Taylor *et al.*, 2000). The authors attribute the formation of spongy clinopyroxene within the diamonds to the presence of cracks and fractures, through which alkali-rich melts or fluids associated with the formation of the spongy clinopyroxene penetrated and interacted with the primary clinopyroxene.

In this study, we conducted a petrological, computed tomography, electron microprobe, Raman spectroscopy, and pMELTS modelling study of six eclogitic clinopyroxene inclusions in six diamonds from the Cullinan (South Africa) mine and Rassolnaya Placer (Urals Mountains, Russia). The studied clinopyroxene inclusions share a common feature in containing various amounts of secondary spongy clinopyroxene, typically around their rims. Considering these inclusions in diamond are well protected from low pressure–temperature alteration, they provide an ideal opportunity for addressing the possible origins of spongy clinopyroxene in mantle-derived samples.

SAMPLES AND METHODS

Diamonds and their mineral inclusions

We studied six diamonds containing clinopyroxene inclusions with spongy textures (Figs 1 and 2, Supplementary Figs S1–S5). These samples are from a suite of diamonds, which has been previously studied for their mineral inclusion compositions (Korolev *et al.*, 2018a; Korolev *et al.*, 2018b; Korolev *et al.*, 2023). Mineral inclusions were exposed on the diamonds surfaces by polishing with diamond-impregnated steel scaife at the University of British Columbia, Canada.

Four diamonds (Cln-268, Cln-285, Cln-320, and Cln-481; Fig. 1a–c and f) are from the Cullinan (former Premier) kimberlite pipe, Kaapvaal Craton. Two diamonds (U-345 and U-530; Fig. 1d and e) are from the Rassolnaya alluvial deposit in the Krasnovishersky region of the Urals, Russia. The weights of the host Cullinan diamonds range between 4.5 and 7.7 mg (0.0225–0.0385 ct), while those from Rassolnaya are 47.3 mg (0.24 ct; U-530) and 128.7 mg (0.64 ct; U-345). All diamonds are colourless and have either dodecahedral (U-345, U-530, Cln-268, Cln-320, and Cln-481) or octahedral (Cln-285) habit (Supplementary Table S1). A detailed characterisation of the Cullinan diamonds, including FTIR, photoluminescence, and morphological features has been reported by Korolev *et al.* (2018a). The morphology of diamond U-530 is reported by Rakin (2013) (sample number 20530 in the original paper). The primary host rock of the Rassolnaya diamonds remains unclear and, like many other placers in the region, has not been reliably identified (Khachatryan *et al.*, 2004; Sobolev *et al.*, 2019; Vasilev *et al.*, 2019). The Rassolnaya Placer is an alluvial deposit occurring within a karst depression at the contact of Vendian–Cambrian terrigenous rocks of the Churochnaya Formation (PR_3–$Є_{er}$) and Silurian carbonate rocks of the Kolchim Formation (Nikulin, 2022). The depression is predominantly filled with clayey and terrigenous rocks of Palaeogene–Neogene age, including diamond-bearing sediments formed at the expense of erosion of intermediate diamond collectors (Ordovician, Lower Silurian and Lower Devonian coastal-marine, and deltaic deposits) (Nikulin, 2022). Diamonds are concentrated mainly in Miocene alluvium (Grahanov *et al.*, 2007).

Diamonds in this study containing spongy clinopyroxene belong to the eclogite paragenesis based on garnet and clinopyroxene inclusion chemistry (<0.3 wt % Cr_2O_3). All but one sample (U-530) contains multiple mineral inclusions. Both diamonds Cln-268 and Cln-285 also contain one exposed clinopyroxene

Table 1: Major element composition (in wt %) of primary cores and spongy rims of the studied clinopyroxene inclusions

Sample	Area	Av. of	SiO_2	1 s	TiO_2	1 s	Al_2O_3	1 s	Cr_2O_3	1 s	FeO	1 s	MnO	1 s	MgO	1 s	CaO	1 s	Na_2O	1 s	K_2O	1 s	NiO	1 s	Total
Ural diamonds																									
U-345	Core	3	55.20	0.28	0.61	0.03	8.94	0.01	0.08	0.06	5.30	0.07	0.10	0.02	13.75	0.03	10.43	0.03	5.15	0.03	0.34	0.01	0.10	0.02	100.00
	Rim 1	1	54.19	–	0.69	–	5.45	–	0.20	–	–	–	0.09	–	16.23	–	13.88	–	1.87	–	0.41*	–	0.10	–	98.85
	Rim 2	1	53.76	–	0.78	–	4.97	–	<MDL	–	–	–	0.13	–	16.87	–	15.36	–	1.72	–	0.33*	–	0.10	–	99.92
	Rim 3	1	54.46	–	0.81	–	3.48	–	<MDL	–	–	–	0.17	–	18.25	–	14.37	–	2.22	–	<MDL	–	0.09	–	99.99
	Rim 4	1	54.16	–	0.80	–	3.15	–	0.15	–	–	–	0.10	–	18.50	–	14.94	–	1.79	–	<MDL	–	0.10	–	100.01
U-530	Core	2	55.93	–	0.55	–	14.86	–	0.07	–	–	–	<MDL	–	6.19	–	9.15	–	8.07	–	0.23	–	<MDL	–	99.94
	Rim 1	1	54.34	–	0.40	–	11.08	–	0.14	–	–	–	<MDL	–	8.24	–	14.54	–	4.22	–	<MDL	–	<MDL	–	99.99
	Rim 2	1	52.62	–	0.81	–	10.32	–	<MDL	–	–	–	0.19	–	9.23	–	15.33	–	3.91	–	<MDL	–	<MDL	–	99.94
	Rim 3	1	51.72	–	0.74	–	10.97	–	<MDL	–	–	–	<MDL	–	9.35	–	16.05	–	3.93	–	<MDL	–	<MDL	–	100.00
	Rim 4	1	52.24	–	0.77	–	10.33	–	<MDL	–	–	–	<MDL	–	9.44	–	15.60	–	3.92	–	<MDL	–	<MDL	–	99.94
	Rim 5	1	53.23	–	0.81	–	11.26	–	0.19	–	–	–	<MDL	–	9.13	–	14.55	–	4.25	–	<MDL	–	<MDL	–	99.98
	Glass 1	1	62.35	–	0.29	–	20.19	–	<MDL	–	–	–	<MDL	–	0.94	–	2.93	–	7.91	–	0.82	–	<MDL	–	99.98
	Glass 2	1	60.47	–	0.46	–	19.74	–	0.10	–	–	–	0.11	–	1.76	–	4.95	–	7.62	–	0.67	–	<MDL	–	100.00
	Glass 3	1	62.86	–	0.42	–	20.85	–	<MDL	–	–	–	<MDL	–	1.23	–	2.21	–	8.04	–	0.71	–	<MDL	–	100.00
Cullinan diamonds																									
Cln-320	Core	3	53.97	0.19	0.22	0.01	7.60	0.04	0.14	0.07	5.68	0.03	0.09	0.02	13.50	0.07	14.89	0.06	3.68	0.08	0.25	0.01	0.12	0.03	100.12
	Rim 1	1	53.29	–	0.21	–	6.50	–	<MDL	–	5.97	–	0.14	–	14.54	–	15.71	–	2.81	–	0.28*	–	0.11	–	99.56
	Rim 2	1	52.70	–	0.18	–	4.03	–	0.20	–	6.16	–	0.13	–	16.73	–	18.43	–	1.56	–	<MDL	–	0.09	–	100.21
Cln-268	Core	3	54.86	0.05	<MDL	0.03	7.04	0.01	<MDL	0.06	2.41	0.04	<MDL	0.01	13.41	0.05	19.67	0.19	3.22	0.05	0.08	0.01	<MDL	–	100.70
	Rim 1	1	55.11	–	<MDL	–	5.14	–	0.15	–	2.51	–	<MDL	–	14.96	–	21.96	–	1.05	–	<MDL	–	0.10	–	100.97
	Rim 2	1	54.15	–	<MDL	–	3.72	–	0.11	–	2.59	–	<MDL	–	16.09	–	23.71	–	0.92	–	<MDL	–	<MDL	–	101.29
Cln-285	Core	3	53.35	1.10	0.52	0.05	8.41	0.10	0.07	0.02	7.37	0.01	0.12	0.02	11.01	0.17	15.25	0.05	3.69	0.06	0.10	0.01	<MDL	–	99.90
	Rim 1	1	53.50	–	0.52	–	7.84	–	<MDL	–	7.27	–	0.14	–	11.86	–	15.79	–	2.98	–	0.08*	–	<MDL	–	99.98
	Rim 2	1	52.72	–	0.57	–	6.23	–	0.15	–	7.03	–	0.10	–	13.68	–	18.01	–	1.35	–	<MDL	–	<MDL	–	99.85
	Rim 3	1	53.32	–	0.63	–	5.61	–	0.08	–	5.65	–	<MDL	–	14.38	–	19.32	–	1.20	–	<MDL	–	<MDL	–	100.20
Cln-481	Secondary 1	1	53.24	–	0.07	–	0.32	–	0.33	–	5.43	–	0.20	–	15.74	–	23.84	–	1.11	–	0.09	–	0.07	–	100.44
	Secondary 2	1	53.64	–	0.08	–	0.45	–	0.21	–	5.71	–	0.17	–	15.54	–	22.66	–	1.13	–	0.17	–	<MDL	–	99.76
	Secondary 3	1	55.31	–	0.07	–	0.52	–	0.16	–	5.17	–	0.18	–	15.77	–	22.92	–	1.03	–	0.25	–	<MDL	–	101.38
	Spot-1 (Phl)	1	49.88	–	0.32	–	5.47	–	<MDL	–	9.31	–	0.13	–	24.66	–	3.42	–	0.29	–	6.52	–	<MDL	–	100.00
	Spot-2 (Phl)	1	48.44	–	0.96	–	6.33	–	<MDL	–	9.33	–	0.22	–	22.56	–	4.13	–	0.30	–	7.72	–	<MDL	–	99.99

<MDL, below minimum detection level; Phl, phlogopite; 1 s, one standard deviation
*Values are likely contaminated by glass.

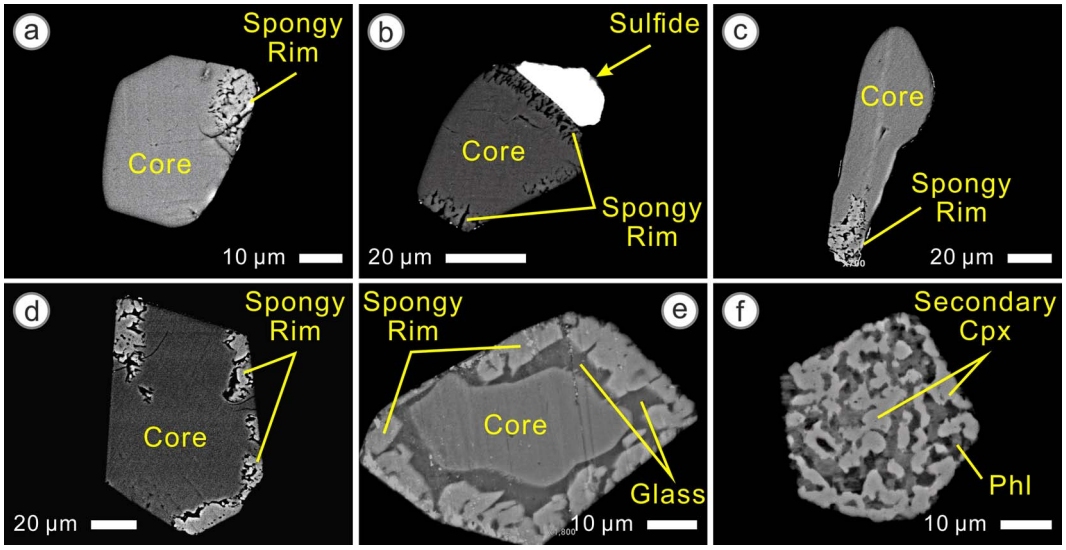

Fig. 1. Back-scattered electron (BSE) images of the studied clinopyroxene inclusions in diamonds. Images (a) Cln-268, (b) Cln-285, (c) Cln-320, (d) U-345, (e) U-530, and (f) Cln-481. Cln-481 shows a complete transformation of primary clinopyroxene into spongy clinopyroxene and phlogopite with no core clinopyroxene preserved. Cpx, clinopyroxene; Phl, phlogopite; Gl, glass.

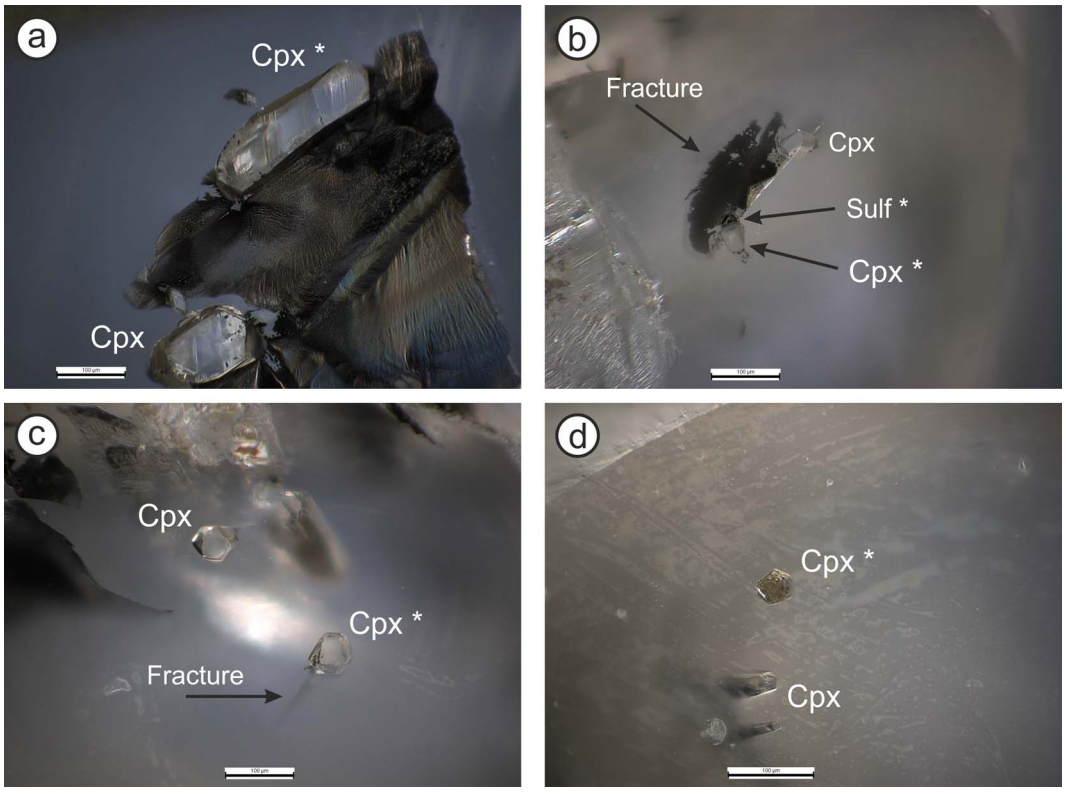

Fig. 2. Representative spongy-rimmed clinopyroxene (Cpx) inclusions in the studied diamonds: a) U-345; b) Cln-285; c) Cln-268; and d) Cln-481, which has been completely transformed into secondary clinopyroxene. ∗ delineates the exposed inclusions on the surface.

without spongy textures. These pristine inclusions have identical compositions to the cores of the other clinopyroxene inclusions in the same diamond that have spongy rims (Supplementary 1 in Korolev *et al.*, 2018b).

Diamond Cln-320 has three clinopyroxene and two garnet inclusions exposed, with one of the clinopyroxenes having a spongy texture on its rim. The composition of the unaltered core of this inclusion is nearly identical to the other two clinopyroxene inclusions (Korolev *et al.*, 2018b). The garnets are pyropes with small amounts of almandine and grossular end-members (Korolev *et al.*, 2023). Based on major elements in garnet and clinopyroxene, P–T calculations indicate equilibration at 6.2–6.4 GPa and 1370–1400°C (Korolev *et al.*, 2023).

Diamonds Cln-268, Cln-285, and Cln-481 also contain sulfide inclusions. Cln-268 has three exposed sulfides with intermediate sulfide solid solution compositions containing Cu (17.9–25.3 wt %), Ni (1.1–8.1 wt %), Co (up to 1.5 wt %), and Pb (0.2–0.3 wt %) (Supplementary Table S2). In Cln-285, clinopyroxene

forms a touching inclusion with pyrrhotite containing Ni (4.3–4.8 wt %), Cu (0.5–1.4 wt %), Pb, and Cr (<0.2 wt % each) (Fig. 1b, Supplementary Table S2). The presence of an unexposed sulfide inclusion in Cln-481 has been confirmed by Raman spectroscopy. Diamond U-345 contains only one exposed spongy-rimmed clinopyroxene. Raman spectroscopy indicates the presence of eight clinopyroxenes and one garnet unexposed within this diamond.

SEM–EDS

The textures of the exposed mineral inclusions in diamonds were studied using a Jeol JSM-IT100 InTouchScope™ scanning electron microscope (SEM) at University College Cork, Ireland. The microscope is equipped with a 25-mm^2 solid-state energy dispersive X-Ray spectroscopy (EDS) detector for X-ray analysis. Analytical conditions included an accelerating voltage of 20 kV, 60% probe current, objective aperture of 30 μm, and working distance of 10 mm. For analysis, samples were coated with 15 nm of carbon.

The chemical composition of the spongy clinopyroxene and glass of the inclusion in diamond U-530 was determined by SEM-EDS at the Institute of Precambrian Geology and Geochronology of the Russian Academy of Science (RAS), Saint-Petersburg, Russia using a scanning electron microscope JEOL JSM-6510LA with an energy dispersive attachment JED-2200, an accelerating voltage of 20 kV, a beam current of 5 nA, a spot size of ∼3 μm, and working distance 11 mm. Synthetic oxides, metals, and natural minerals were used as standards. The ZAF algorithm has been applied to correct for matrix effects.

EPMA

The chemical composition of all inclusions (except U-530) was studied by Wavelength Dispersive Spectroscopy (WDS) using a JEOL JXA-8230 electron microprobe at the Hebrew University of Jerusalem (HUJI), Israel. Inclusion U-530 was lost during sample preparation following EPMA analysis at the University of British Columbia; therefore, we were unable to repeat further major element analysis at HUJI. All samples were carbon-coated before analysis. Operating conditions were 15 kV excitation voltage, 15 nA beam current, 30 s peak count time, 15 s background count time, and a ∼2–5-μm spot diameter. Detection limits for the different oxides measured were below 0.07 wt %. For clinopyroxene, the following standards, X-ray lines, and crystals were used: bustamite, Mn-Kα, LIFL; chromite, Cr-Kα, PETJ; chromite, Fe-Kα, LIFH; diopside, Ca-Kα, PETL; diopside, Mg-Kα, TAPH; diopside, Si-Kα, TAP; jadeite, Al-Kα, TAP; jadeite, Na-Kα, TAPH; kaersutite, Ti-Kα, LIFH; pentlandine, Ni-Kα, LIFH; sanidine, K-Kα, PETL.

For inclusion U-530, the core clinopyroxene was measured at the University of British Columbia, Canada using a CAMECA SX-50 electron microprobe. All elements were analysed with a beam current of 20 nA, an acceleration voltage of 15 kV, 20 s count time, and 10 s background count time. Longer counts (40 s on the peak and 20 s on the background) were used for K in pyroxene. The beam diameter was approximately 5 μm. For pyroxene analyses, the following standards, X-ray lines, and crystals were used: albite, Na-Kα, TAP; kyanite, Al-Kα, TAP; diopside, Mg-Kα, TAP; diopside, Si-Kα, TAP; orthoclase, K-Kα, PET; diopside, Ca-Kα, PET; rutile, Ti-Kα, PET; synthetic magnesiochromite, Cr-Kα, LIF; synthetic rhodonite, Mn-Kα, LIF; synthetic fayalite, Fe-Kα, LIF. Detection limits for the different oxides measured were below 0.07 wt %.

Raman spectroscopy

Raman spectra of mineral inclusions were obtained at room temperature using a Renishaw InVia Qontor confocal Raman microscope equipped with a 532 nm diode-pumped solid-state laser (DPSS) and a Peltier cooled (−70°C) near-infrared enhanced deep depletion CCD detector at University College Cork, Ireland. Calibration was achieved via an internally mounted silicon standard at 520.5 cm^{-1}. Measurements used a × 50 LWD objective, laser residence times of 10–25 s and 2–4 acquisitions per sample. The spectral resolution limit was 0.02 cm^{-1} and spatial resolution was ∼1.2 μm. Spectra were processed using Renishaw WiRE 5.5 to remove the cosmic-ray peaks and in OriginPro software for baseline subtraction, peak positioning, and smoothing. In this study, Raman spectroscopy is a qualitative method that allows us to determine the presence of volatile components, but not to quantify their concentration.

CT-scan

X-ray micro-tomography (μCT) data were collected for two clinopyroxene inclusions and one fracture from diamond U-345 at the American Museum of Natural History (AMNH) Microscopy and Imaging Facility using a ZEISS Xradia 630 Versa μCT system (Supplementary video files S1, S2, and Figs S7–S15). One inclusion is exposed on the diamond surface (Fig. 1d) and the other is inside the diamond (Fig. 2a). The fracture is on the other side of the diamond U-345 unrelated to the studied inclusions. The Xradia instrument operated with a current of 125 μA and potential of 60.0 kV (6.5 W power) to generate polychromatic X-rays with a tungsten anode X-ray tube. The objective used was 40X-P and source filter LE1. Data were collected with a resolution (pixel size) of 0.345 μm/voxel edge.

pMELTS modelling

To constrain the P–T parameters of the spongy clinopyroxene rims surrounding pristine primary cores and to assess whether melting of primary clinopyroxene occurred in a closed system, we performed geochemical modelling using the 5.6.1 MS Excel version of pMELTS software (Ghiorso *et al.*, 2002; Gualda & Ghiorso, 2015). Based on the textural features and chemical compositions, we assume the cores of clinopyroxene inclusions represent a starting composition (primary clinopyroxene from here onwards), while the spongy clinopyroxene at the rims is a residue after partial melting of the primary clinopyroxene. In some diamonds (U-530 and inclusions described by Taylor *et al.*, 2000) as well as in many mantle xenoliths (Misra *et al.*, 2004), spongy clinopyroxene also coexists with detectable glass/melt (see discussion below), which represents a product of partial melting of the primary clinopyroxene.

For the purpose of pMELTS modelling, we make the assumption that the entire inclusion is a closed (or nearly closed) system with regard to material exchange. The primary clinopyroxene is then melted over a broad range of pressures (0–4 GPa) and temperatures (600–1400°C) over a grid of 0.05 GPa and 50°C, at −3.7 log units relative to FMQ (oxygen fugacity relative to fayalite–magnetite-quartz buffer), to produce melt, residual spongy clinopyroxene, and in some scenarios an additional phase. The $\Delta \log fO_2$(FMQ) value of −3.7 was chosen based on previous work on the redox state of mantle eclogite xenoliths from the Kaapvaal Craton, which all have similar ranges. In detail, eclogites from the Lace kimberlites, close to the Cullinan pipe, record $\Delta \log fO_2$(FMQ) values from −1.3 to −4.6; median of −3.7 (Aulbach *et al.*, 2017). Values of −1.2 to −4.0; median of −2.5 are reported for Bellsbank

eclogites (Smart *et al.*, 2021). Finally, values of −1.5 to −5.3; median of −3.8, are reported for eclogites from Jagersfontein, Kimberley (Kamfersdam) and Roberts Victor pipes (Burness *et al.*, 2020).

Overall, our samples are comprised of three phases only: primary clinopyroxene, spongy clinopyroxene, and rare glass. Even when visible, it is not possible to accurately determine the glass composition due to its small size, except for the inclusion in diamond U-530, which has a large melt pool. For pMELTS calculations, we limit the output of the modelling to two phases: clinopyroxene and melt. However, at some P–T conditions, to satisfy equilibrium, the presence of an additional mineral phase is required as a product of melting. This is usually either a nepheline solid solution compound ('Neph ss') or an additional clinopyroxene ('Cpx II'; Supplementary Table S3). Taking into account the absence of any phases besides clinopyroxene and glass in the studied spongy rims, we used 'Neph ss' as a qualitative indicator of the presence of another phase in the melting products, without investigating in detail each of the possible multiple equilibria.

Following the pMELTS modelling, we matched the compositions of modelled clinopyroxenes with the natural spongy clinopyroxenes from inclusions in diamonds (Supplementary Tables S4–S9). For this, we allow an empirically selected discrepancy of no more than 15% for each oxide (SiO_2, Al_2O_3, MgO, CaO, Na_2O, and FeO). This discrepancy is chosen mainly to satisfy both major (such as SiO_2, Al_2O_3, MgO, etc.) oxides, for which 10% discrepancy would be sufficient, and relatively minor (such as Na_2O) oxides, for which 20% discrepancy would be more favourable.

Taking into account the temperature range of 850–1300°C and the pressure range of 0.5–2.7 GPa obtained from the pMELTS modelling (Supplementary Table S3), as well as the studies by Ghiorso *et al.* (2002), Jennings & Holland (2015), and Otto *et al.* (2023), the uncertainty in temperature for pMELTS calculations is estimated to be 50°C, while the uncertainty in pressure is approximately 0.1 GPa.

Notably, the modelled pMELTS ranges of pressure and temperature (Supplementary Table S3) show the most likely conditions under which melting occurred. These estimates should not be taken as exact melting conditions and do not necessarily imply that melting occurred over the entire temperature and pressure range shown. These estimates are indicative of the P–T range outside of which the melting is highly unlikely.

Clinopyroxene-only thermobarometry

The crystallisation temperature and pressure of each spongy clinopyroxene was calculated using the clinopyroxene-only barometer and thermometer of Putirka (Putirka, 2008, eqn. 32b [barometer] and eqn. 32d [thermometer]). The thermobarometer has been calibrated mainly over a range of 900–1600°C and 0.0–3.2 GPa using experimental data, with an uncertainty of 87°C in temperature and 0.26 GPa in pressure (Putirka, 2008). We have restricted our results to below 2.0 GPa as the accuracy of the barometer decreases at higher pressures (see Figs. 8c and 9h from Putirka, 2008). The Excel spreadsheets used for the calculations are provided in the supplemental materials of Neave & Putirka (2017). For each clinopyroxene composition, the equations were solved iteratively ($n = 200$) to converge on a final temperature and pressure (i.e. the solution of one equation, temperature or pressure, was used as one of the inputs for the other equation until the change between iterations was less than 0.001). Reported results were calculated for melt compositions containing 0.5 wt % H_2O. A range of 0–2 wt % was also explored but had little effect on the calculations. Additionally, we applied the thermobarometer by Jorgenson *et al.* (2022), which is based on machine learning and employs various models reported in the literature. This thermobarometer was developed by compiling a large dataset of experimentally obtained clinopyroxene and its equilibrium liquid compositions and applying a series of algorithm-based predictive models, and calibrating it using a large number of experimental results at 0–3 GPa and 800–1500°C.

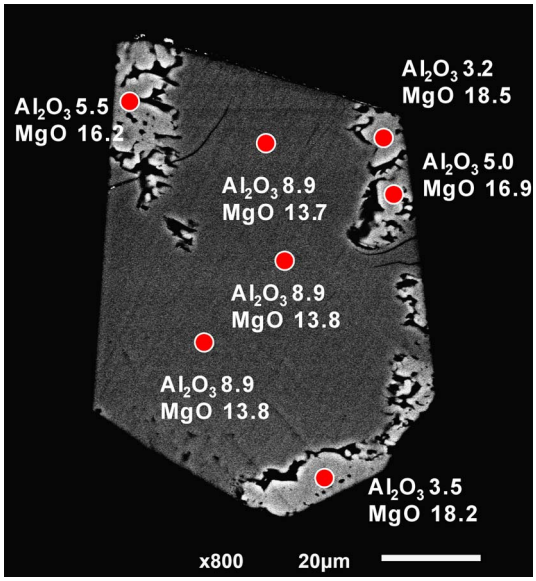

Fig. 3. BSE-image of a clinopyroxene inclusion in diamond U-345 displaying variations in Al_2O_3 and MgO (wt %) across the grain. The core area is largely homogeneous, while the rim areas, characterised by spongy textures, exhibit variable compositions.

RESULTS

Textures of spongy clinopyroxene

Except for one sample, all spongy clinopyroxene inclusions in this study have cores with primary textures and compositions and rims that comprise spongy textures, which consist of secondary clinopyroxene with spongy or cracked textures and adjacent melt pockets (Figs 1 and 3; Supplementary Figs S1–S5 and S7–S14, and Supplementary video files S1 and S2). The six samples show differing degrees of melt formation. In four of the samples (Cln-268, Cln-285, Cln-320, and U-345), melt pockets within the spongy rims are too small to measure. However, the presence of melt pockets can be inferred from elevated potassium contents in a number of EPMA analyses of spongy clinopyroxene. These K-rich (up to ~0.41 wt % of K_2O) compositions are similar to glass occurring adjacent to spongy clinopyroxene in diamond U-530. The spongy rim of the clinopyroxene inclusion in this diamond consists of two clearly distinguishable phases—secondary clinopyroxene and glass (Fig. 1e and Supplementary Fig. S1). Inclusion Cln-481 has been completely transformed into secondary clinopyroxene and coexists with phlogopite (Fig. 1f). The small sizes of each of these minerals prevented us from determining their compositions by EPMA.

The CT-scan analysis of inclusions in sample U-345 revealed that spongy textures occur only on the rims of the inclusions and are mainly concentrated along the edges of crystal faces (Supplementary video files S1, S2, and Figs S7–S14).

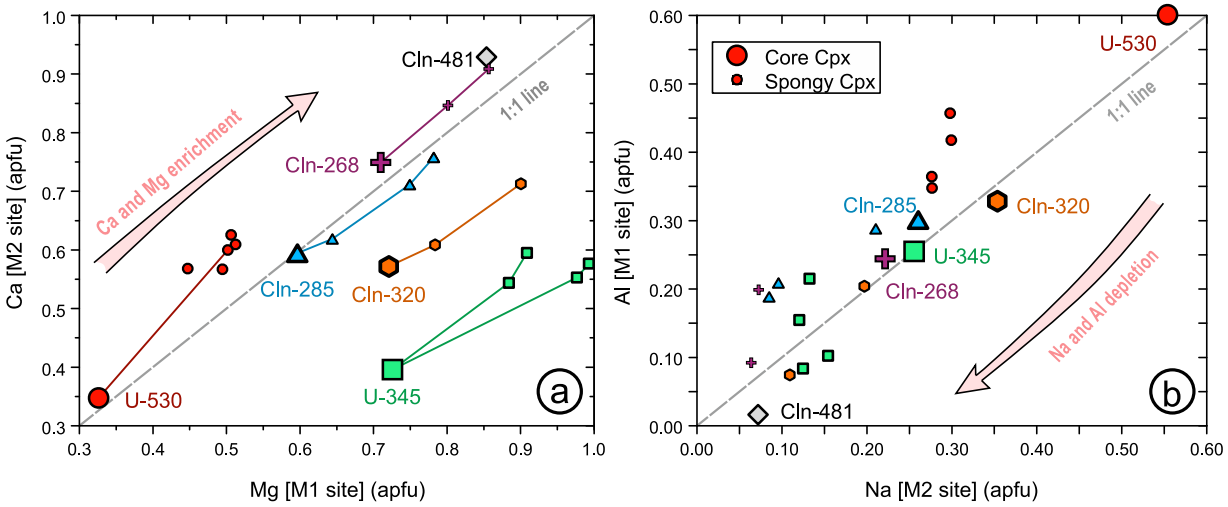

Fig. 4. Major element compositions of clinopyroxene cores and spongy rims from the studied inclusions. Cores are depicted by large symbols, while their spongy counterparts are represented by corresponding small symbols. Sample Cln-481, a fully altered clinopyroxene, is an example of extreme Na and Al depletion alongside Mg and Ca enrichment. Apfu, atoms per formula unit.

Optical observations show that some of the studied spongy clinopyroxene inclusions are associated with fractures within the diamonds. Some of the fractures are filled with graphite and/or sulfide material (Fig. 2a and b), while some of them are empty (Fig. 2c).

It should be emphasised that there is no direct correlation between the presence of visible fractures and inclusions with spongy textures. For instance, diamond Cln-285 shows both a spongy-rimmed clinopyroxene and an unmodified clinopyroxene inclusion in conjunction with the same fracture (Fig. 2b). SEM and EPMA measurements show that the unmodified clinopyroxene is homogeneous in terms of major element composition. Moreover, in other cases, we observe unaltered homogeneous inclusions in association with fractures. Also, the completely altered Cln-481 inclusion does not have any visible nearby feeder fractures—fractures with visible secondary mineralisation that could indicate an influx of external material (Fig. 2d).

Major element composition

Major element compositions of the unaltered primary clinopyroxene cores and associated spongy clinopyroxene are presented in Table 1. The primary clinopyroxenes with homogeneous compositions are eclogitic omphacites (<0.1 wt % of Cr_2O_3) with jadeite contents between 20.0 and 57.5% (Na_2O 3.2–8.1 wt % and Al_2O_3 7.0–14.9 wt %). The compositions of the secondary spongy clinopyroxene are either augite (U-345, Cln-285, and Cln-320), low-jadeite omphacite (U-530, Cln-285, and Cln-320), or aluminium diopside (Cln-268). The Cln-481 inclusion has been completely transformed into secondary clinopyroxene of Fe-rich diopside composition (Fig. 1f and Table 1). There is no spatial systematic order, zoning, or pattern of changes in the chemical composition of spongy clinopyroxene. This secondary clinopyroxene is characterised by extremely heterogeneous compositions in different areas of the inclusion. For example, for the inclusions in sample U-345 (Fig. 3), compared to the homogeneous core, the spongy rim exhibits significant differences in MgO content (13.7–13.8 wt % vs. 16.2–18.5 wt %), Al_2O_3 (8.9 wt % vs. 3.2–5.5 wt %), and other oxides (Table 1).

Nevertheless, in all inclusions the spongy clinopyroxene is depleted in Na and Al (Na_2O of 0.9–4.2 wt %, Al_2O_3 of 3.2–11.3 wt %) and enriched in Mg and Ca (MgO of 8.2–18.5 wt %, CaO of 13.9–23.7 wt %) in comparison with the primary homogeneous omphacite cores (Figs 4, 5, Supplementary Fig. S6 and Supplementary Tables S4–S8). Sample Cln-481, with a spongy texture, which has completely transformed into secondary diopside, has the most depleted composition of all samples with lowest Na and Al and highest Mg and Ca values: Na_2O 1.0–1.1 wt %; Al_2O_3 0.3–0.5 wt %; MgO 15.5–15.8 wt %; CaO 22.7–23.8 wt %. The enrichment in the diopside component during transformation from primary to spongy clinopyroxene for each sample is evidenced by an almost perfect 1:1 Ca–Mg ratio of cations (Fig. 4a), while the corresponding depletion in the jadeite component has a close to 1:1 ratio of Na and Al (Fig. 4b). The composition of the glass adjacent to spongy clinopyroxene in diamond U-530 (Fig. 1e) is characterised by high silica (60.5–62.9 wt % of SiO_2) and alkali content (7.6–8.0 wt % of Na_2O and up to 0.8 wt % of K_2O) (Table 1).

Raman measurements of volatile phases in core and spongy clinopyroxene

Raman measurements of the primary cores and spongy rims for the exposed clinopyroxene inclusions between wavenumbers of 1370–4500 cm^{-1} revealed the presence of C–H (2779–3129 cm^{-1}, Socrates, 2004), C=C (1500–1713 cm^{-1}, Socrates, 2004), $X \equiv Y$, $X = Y = Z$; X, Y, and Z may represent any of the atoms C, N, O and S (1842–2355 cm^{-1}, Eremets *et al.*, 2004, Knippers *et al.*, 1986, Sampathkumar *et al.*, 2019), and $(CH_4)n(H_2)m$ (4212–4242 cm^{-1}, Kolesnikov *et al.*, 2009, Somayazulu *et al.*, 1996) bands (Fig. 6 and Supplementary Table S10). The volatiles are likely located either in microinclusions within the pyroxenes or as defects in the crystal structure. Raman and gas chromatography–mass spectrometry studies of inclusions in diamonds show that these bands can be associated with dozens of different compounds such as aliphatic, cyclic, and oxygenated hydrocarbons, heterocyclic and sulfonated groups and many others (Sobolev *et al.*, 2019). In the studied inclusions, the position of these bands varies slightly from sample to sample (Fig. 6 and Supplementary Table S10). However, within the same sample, the sets of observed Raman bands are nearly identical in the primary core and spongy rim parts. This suggests that the core and spongy parts of the clinopyroxene inclusions have the same suite of volatile components. More importantly, it indicates there is no influx of volatile components

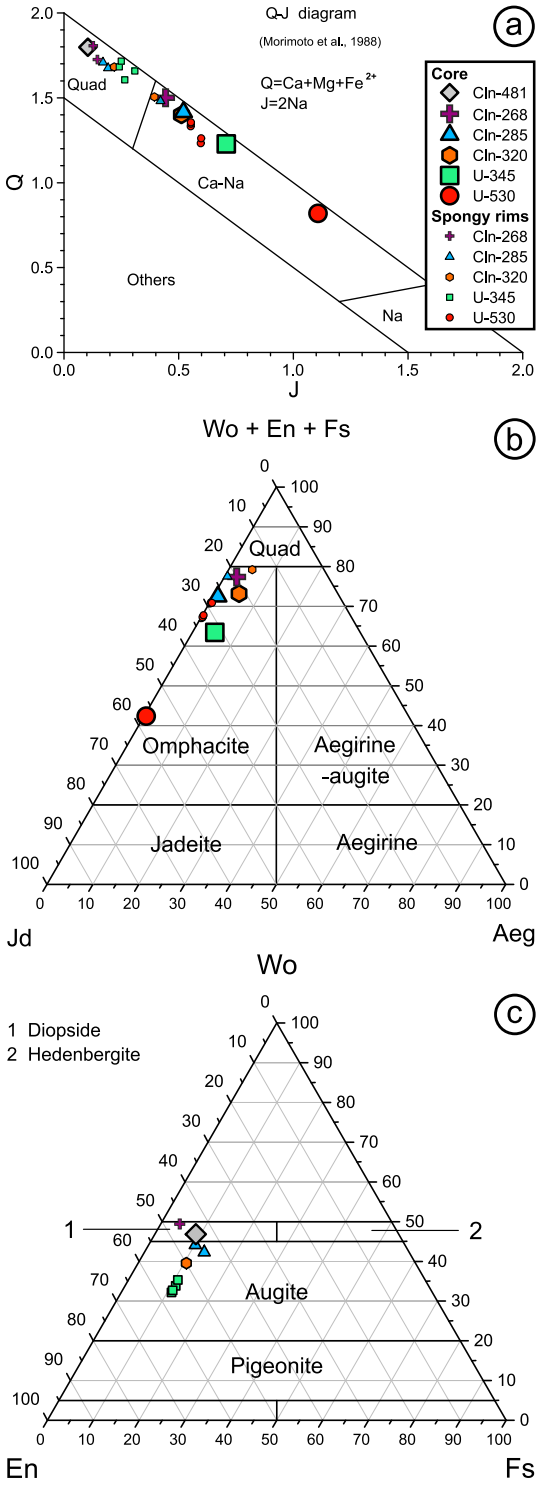

Fig. 5. Chemical compositions of the studied clinopyroxene inclusions. a) Q-J diagram (Morimoto *et al.*, 1988), where Q = Ca + Mg + Fe^{2+} (apfu) and J = 2 × Na (apfu). b) Classification diagrams for Ca-Na pyroxenes (Morimoto *et al.*, 1988). c) Classification diagrams for Ca-Fe-Mg pyroxenes (Morimoto *et al.*, 1988). Mineral symbols according to Warr (2021): Aeg, Aegirine [$NaFe^{3+}_2(SiO_3)_2$], En, Enstatite [$Mg_2(SiO_3)_2$], Fs, Ferrosilite [$Fe^{2+}_2(SiO_3)_2$], Jd, Jadeite [$NaAl(SiO_3)_2$], Wo, Wollastonite [$Ca_2(SiO_3)_2$].

to the newly formed spongy clinopyroxene, compared to those observed in the primary part of the clinopyroxene inclusion (Fig. 6).

DISCUSSION

Occurrence of spongy clinopyroxene as an inclusion in diamond

To deduce the formation of clinopyroxene with spongy textures trapped in diamond, it is necessary to address whether the spongy clinopyroxene was captured in the diamond together with primary clinopyroxene, or formed within the diamond after encapsulation. This also has implications for the formation conditions of spongy clinopyroxene in other mantle lithologies. The majority of pristine mineral inclusions encapsulated in diamond are protogenetic, having formed in the surrounding mantle prior to entrapment in a growing diamond (Bruno *et al.*, 2024). The characteristics of the clinopyroxene inclusions in diamond in this study are consistent with this interpretation. However, the spongy-textured clinopyroxene associated with pockets of melt forming on the rims of the primary clinopyroxene indicate subsequent processes were superimposed on these inclusions following their entrapment in diamond.

Although a deep mantle origin for spongy clinopyroxene is not completely excluded, regardless of its paragenesis (peridotitic or eclogitic), most studies attribute its formation to a low-pressure regime (<2 GPa), well outside of the stability field of diamond (Spetsius & Taylor, 2002; Ma *et al.*, 2015; Bussweiler *et al.*, 2016; Pan *et al.*, 2018). The reasons behind this are the following:

- the presence of porous spongy textures with a lot of voids around them does not coincide with a high-pressure origin (Ma *et al.*, 2015);
- a diopsidic composition, which is significantly more refractory, is usually formed at a lower pressure compared to the initial high-Na and high-K omphacitic clinopyroxene (Hill *et al.*, 2011);
- pressures obtained for most of the reported spongy clinopyroxene are <2.7 GPa regardless of their paragenesis (Ionov *et al.*, 1994; Spetsius & Taylor, 2002; Taylor & Anand, 2004; Lu *et al.*, 2015; Bussweiler *et al.*, 2016; Pan *et al.*, 2018; Chien *et al.*, 2024).
- for mantle xenoliths, spongy clinopyroxene usually forms wide (hundreds of microns) coronas around the primary clinopyroxene. Thus, it is unlikely that diamond could capture both primary and spongy clinopyroxene on a microscale when grain sizes of each are substantially larger.

Undoubtedly, the spongy clinopyroxene represents the residue of partial melting of the primary clinopyroxene. This is supported by the following evidence:

- texturally, it is commonly observed on the rims of the primary clinopyroxene (though in some cases it forms along fractures within the inclusions) and it is always accompanied by small concentrations of alkali-rich melt in the pockets around the spongy texture (Fig. 1e, *e.g.*, Misra *et al.*, 2004; Pan *et al.*, 2018).
- compositionally, spongy clinopyroxene is significantly more refractory than the primary clinopyroxene (Figs 4 and 5; Table 1), and hence cannot be a product of fractional crystallisation from the melt produced by primary clinopyroxene.

The P–T range of melting temperatures can be roughly estimated through element partitioning, specifically Na and Al. The clinopyroxene-only thermobarometers of Putirka (2008) that utilise Na and Al concentrations of clinopyroxene, can be used to estimate the crystallisation P–T conditions for a sample without knowing the composition of the liquid from which the clinopyroxene crystallised. This is useful in this scenario where the melt composition evolved over time (*e.g.*, during kimberlite

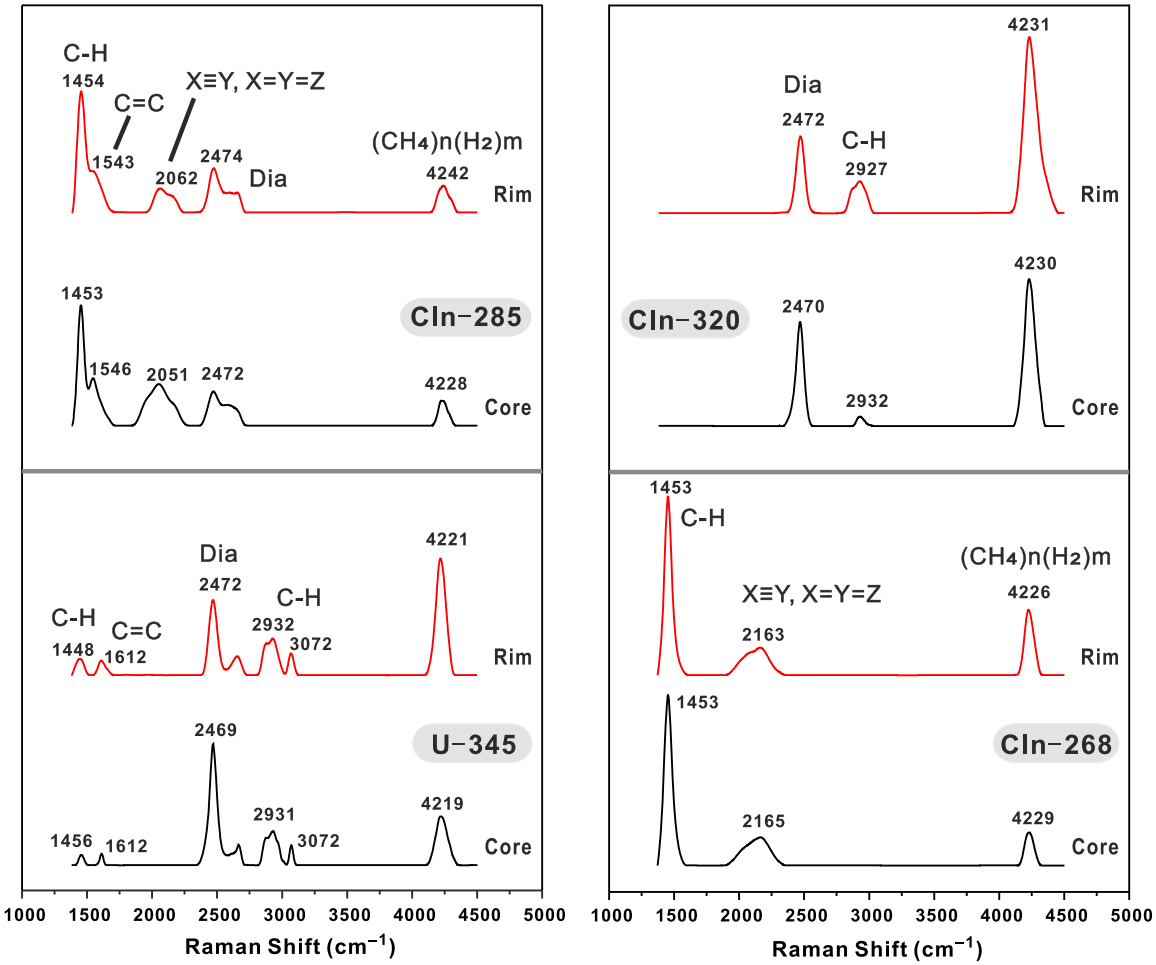

Fig. 6. Representative Raman spectra of primary cores and spongy rims from the studied clinopyroxene inclusions. *X*, *Y*, and *Z* may be represented by C, N, O and/or S in the $X \equiv Y$, $X = Y = Z$ bands (Knippers *et al.*, 1986; Eremets *et al.*, 2004; Sampathkumar *et al.*, 2019). The numbers correspond to the position of the centres of the peaks (Supplementary table S10). The ~2470 cm^{-1} peak is likely associated with the second-order diamond Raman peak (Solin & Ramdas, 1970).

ascent) and the final melt is likely not equilibrated with any one crystallised clinopyroxene. The thermobarometry results support this interpretation (Table 2) in which all samples, regardless of locality, follow a general trend of decreasing temperature and pressure, from ~1320°C at 1.9 GPa to ~1160 at 0.7 GPa (Fig. 7 and Table 2).

Thermobarometry of Jorgenson *et al.* (2022) supports these results and indicates that the studied spongy clinopyroxene can form under pressures of 1.1–2.1 GPa and temperatures of 968–1275°C (Table 2).

An independent tool for determining the P–T conditions for the formation of spongy clinopyroxene through partial melting of primary clinopyroxene is pMELTS modelling. pMELTS modelling was applied to five inclusions from this study (Cln-268, Cln-285, Cln-320, U-345, and U-530) and three inclusions reported by Taylor *et al.* (2000) (W1, W4, and W14). In order to achieve an imposed compositional constraint of <15% difference for each oxide in measured versus modelled spongy clinopyroxene, the calculated equilibrium pressures reach up to ~2.7 GPa for Cln-320 and range between 0.6 and 2.2 GPa for the other four inclusions (Fig. 7). Interestingly, models that had the neph-ss phase yield pressures of less than 0.8 GPa (Supplementary Tables S4, S6, and S9).

Although the range of P–T conditions produced by pMELTS and clinopyroxene thermobarometry for each sample is very large (Fig. 7 and Supplementary Tables S4–S9), it clearly shows that melting occurred at pressures well outside the stability field of diamond (Fig. 7). The resulting P–T conditions (Supplementary Table S3) also far exceed the equilibrium conditions (905–1450°C, 3.4–6.7 GPa) of mantle xenoliths from the Cullinan pipe (Fig. 7) (Dludla *et al.*, 2006; Viljoen *et al.*, 2009; De Hoog *et al.*, 2010) and P–T parameters obtained for the Cln-320 sample using garnet–clinopyroxene thermobarometry 1370–1400°C and 6.2–6.4 GPa (Korolev *et al.*, 2023). At such high storage temperatures, considering the small size of the clinopyroxene (<100 μm), this would lead to a fairly rapid element diffusivity (*e.g.*, the diffusivities for Fe-Mg roughly from 10^{-18} to 10^{-16} m^2/s, according to Müller *et al.*, 2013). This makes it unlikely for small-scale compositional gradients (core clinopyroxene, spongy clinopyroxene, and melt) to survive long-term mantle storage. Additionally, pressures of melting estimated by pMELTS are well below the pressures of geotherms at relevant geotherm temperatures, indicating that the partial melting of these spongy clinopyroxenes was most likely caused by decompression.

The CT-scan study of two representative inclusions (Supplementary video files S1 and S2) provides additional evidence in favour of melting (modification) of the inclusions after, rather than before, their capture by the diamond. The 3D models show that spongy clinopyroxene is concentrated mainly

Table 2: P–T parameters of spongy clinopyroxene

Sample	Composition	T (°C)	ΔT (°C)	P (GPa)	ΔP (GPa)	T (°C)	ΔT (°C)	P (GPa)	ΔP (GPa)	T (°C)	ΔT (°C)	P (GPa)	ΔP (GPa)	T (°C)	ΔT (°C)	P (GPa)	ΔP (GPa)
	from Table 1	Neave & Putirka (2017)				pMELTS modelling				cpx-only model				liq-cpx model		Jorgenson et al. (2022)	
Ural (this study)																	
U-345	Rim 1	1300	87	1.50	0.26	1110	50	0.95	0.10	1275	73	2.13	0.32	–	–	–	-
	Rim 2	1277	87	1.30	0.26	N/a	N/a	N/a	N/a	1240	73	1.50	0.32	–	–	–	-
	Rim 3	1302	87	1.60	0.26	N/a	N/a	N/a	N/a	1195	73	1.15	0.32	–	–	–	-
	Rim 4	1284	87	1.40	0.26	N/a	N/a	N/a	N/a	1215	73	1.15	0.32	–	–	–	-
	Average	1291	87	1.45	0.26	1110	50	0.95	0.10	1231	73	1.48	0.32	–	–	–	-
U-530	Rim 1	N/a	N/a	N/a	N/a	N/a	N/a	N/a	N/a	1024	73	2.03	0.32	1070	45	1.89	0.27
	Rim 2	N/a	N/a	N/a	N/a	900	50	0.75	0.10	979	73	2.10	0.32	1032	45	1.92	0.27
	Rim 3	N/a	N/a	N/a	N/a	1100	50	1.15	0.10	1017	73	2.03	0.32	1051	45	1.94	0.27
	Rim 4	N/a	N/a	N/a	N/a	N/a	N/a	N/a	N/a	968	73	2.05	0.32	1046	45	1.92	0.27
	Rim 5	N/a	N/a	N/a	N/a	N/a	N/a	N/a	N/a	991	73	2.03	0.32	1080	45	1.83	0.27
Cullinan (this study)																	
Cln-320	Rim 1	N/a	N/a	N/a	N/a	850–1300	50	0.50–2.70	0.10	1210	73	2.00	0.32	–	–	–	-
	Rim 2	1280	87	1.40	0.26	N/a	N/a	N/a	N/a	1156	73	1.31	0.32	–	–	–	-
Cln-268	Rim 1	1321	87	1.80	0.26	N/a	N/a	N/a	N/a	1100	73	1.36	0.32	–	–	–	-
	Rim 2	1164	87	0.70	0.26	1200	50	0.60	0.10	1125	73	1.10	0.32	–	–	–	-
Cln-285	Rim 1	N/a	N/a	N/a	N/a	1200–1250	50	1.60–2.15	0.10	1030	73	2.07	0.32	–	–	–	-
	Rim 2	1318	87	1.90	0.26	1200	50	1.00	0.10	1030	73	1.50	0.32	–	–	–	-
	Rim 3	1307	87	1.80	0.26	N/a	N/a	N/a	N/a	1100	73	1.38	0.32	–	–	–	-
	Average	1313	87	1.85	0.26	–	–	–	–	1053	73	1.65	0.32	–	–	–	-
Udachnaya (Taylor *et al.*, 2000)																	
W1	W1–2	1232	87	1.10	0.26	980–1020	50	0.30–0.35	0.10	1050	73	1.20	0.32	1231	45	1.25	0.27
	W1–6	1231	87	1.20	0.26	1050	50	0.60	0.10	1033	73	1.50	0.32	1256	45	1.50	0.27
	Average	1232	87	1.15	0.26	–	–	–	–	1042	73	1.35	0.32	1244	45	1.38	0.27
W5	W5–2	1281	87	1.80	0.26	–	–	–	–	1080	73	1.53	0.32	1123	45	1.51	0.27
	W5–7	1227	87	1.10	0.26	–	–	–	–	1125	73	1.75	0.32	1136	45	1.53	0.27
	W5–3	1282	87	1.80	0.26	–	–	–	–	1016	73	1.50	0.32	1128	45	1.50	0.27
	Average	1263	87	1.57	0.26	1000–1100	50	0.50–0.80	0.10	1074	73	1.59	0.32	1129	45	1.51	0.27
W14	W14–2	N/a	N/a	N/a	N/a	800–1050	50	0.40–0.75	0.10	1100	73	1.80	0.32	1053	45	1.69	0.27
	W14–3	1261	87	1.40	0.26	800–1050	50	0.40–0.75	0.10	1138	73	1.58	0.32	1040	45	1.55	0.27

The temperature and pressure results are from calculations using Putirka's equations (Putirka, 2008, eqn. 32b [barometer] and eqn. 32d [thermometer]), pMELTS modelling results, and results from the thermobarometer by Jorgenson *et al.* (2022), respectively.

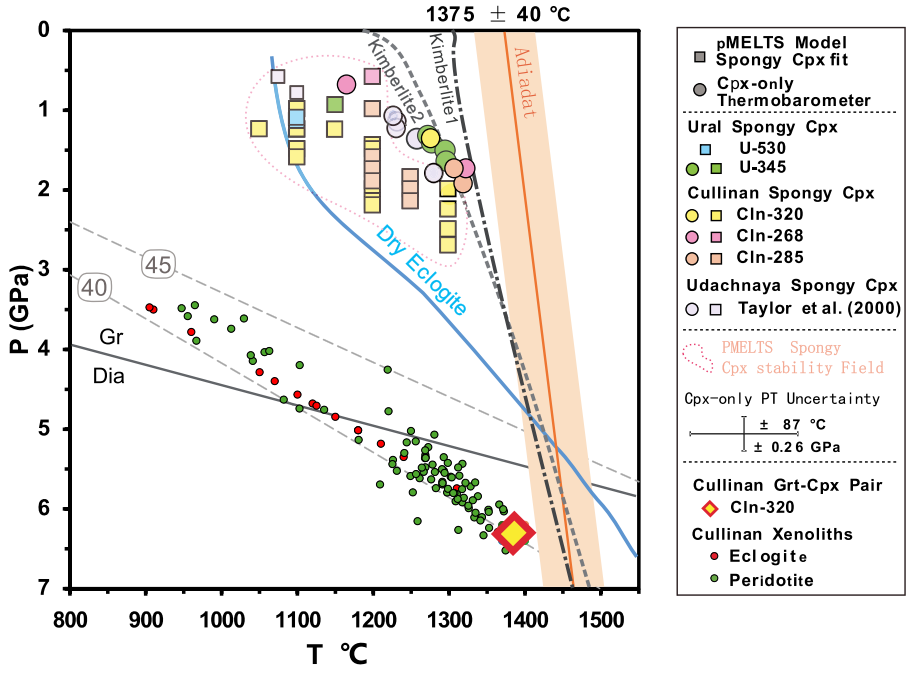

Fig. 7. P–T estimates for the formation conditions of spongy clinopyroxene inclusions in diamond. Squares represent the results of the pMELTS calculation grid search, where compositions closely match measured spongy clinopyroxene from this study and those reported by Taylor *et al.* (2000). The red dashed line surrounding these points is interpreted as the potential P–T range for spongy clinopyroxene crystallisation. Circles represent the results of the clinopyroxene-only thermobarometry, using the Putirka (2008)'s equations 32b as a barometer and 32d as a thermometer. P–T equilibrium estimates for Cullinan peridotite xenoliths are taken from Viljoen *et al.* (2009) and De Hoog *et al.* (2010), while eclogite xenoliths estimates are from Dludla *et al.* (2006) and recalculated by Korolev *et al.* (2018b). The yellow and red squares represent P–T conditions calculated for clinopyroxene-garnet paired (non-touching) inclusion from the same diamond, Cln-320 (Korolev *et al.*, 2018b). The solid orange line represents an ambient mantle adiabat with a surface temperature of 1375 ± 40°C and a temperature gradient of 0.4°C/km (Katsura *et al.*, 2010). The solid blue line denotes the dry eclogite solidus (Yasuda *et al.*, 1994). Model conductive geotherms labelled 40 and 45 (mW/m^2) are after Hasterok & Chapman (2011). The graphite (Gr)–diamond (Dia) phase boundary of Day (2012) is shown by the solid dark grey line. The black dashed lines represent the kimberlite ascent path, which is determined by Kavanagh & Sparks (2009).

along crystal edges. When we consider how spongy textures in mantle xenoliths strongly affect grain rims, making their crystallographic shapes poorly defined, it seems unlikely that diamond inclusions could have been captured with the observed morphological relationship between sponge-like rims and pristine cores (Supplementary video files S1 and S2).

In the case of encapsulation of a spongy-rimmed clinopyroxene, one would expect a random distribution between the two types of clinopyroxene, with one part of the inclusion showing spongy textures and the other comprising a primary core (in varying proportions). However, since spongy clinopyroxene is developed exclusively along the crystal edges, the assumption of clinopyroxene entrapment together with the spongy textures seems unlikely.

'Near-closed' system melting: textural observations

Now that we have established the capture of primary clinopyroxene by the diamond prior to its partially melting upon decompression, we can address the question of whether melting and the formation of spongy clinopyroxene occurred in a chemically 'closed' versus 'open' system while trapped in the diamond. The term near-closed applied in this study refers to a system that is open to the changes in external pressures and temperatures, but closed with respect to the influx or outflux of material from the inclusion. This has direct implications for the style of melting within the diamond and the formation of spongy clinopyroxene as a result of a partial melting of the primary clinopyroxene.

Evidence in support of a near-closed system is the presence of small fractures within the diamonds associated with the studied inclusions (Fig. 2). Given the low-pressure origin of spongy clinopyroxene, the likely trigger for decompression melting within diamond is the presence of a fracture that would allow the inclusion to experience changes in pressure outside of its protective diamond 'capsule'. It is well established that within a closed system, such as a diamond, the retrogression of high-pressure phases to lower pressure counterparts can occur. For instance, with decreasing pressure bridgmanite reverts to orthopyroxene (enstatite), ringwoodite reverts to olivine (Nestola *et al.*, 2023), and majoritic garnet may revert to touching clinopyroxene and lower-pressure garnet (Wilding, 1990; Harte & Cayzer, 2007). Garnet and pyroxenes tend to maintain relatively low internal pressures upon decompression of the diamond on its ascent to Earth's surface (Barron, 2005; Nestola *et al.*, 2011), which is supported by a large number of well-preserved garnet and pyroxene inclusions in diamonds reported in the literature (Stachel & Harris, 2008 and references therein). Therefore, any pressure-related modifications of clinopyroxene inclusions upon diamond ascent are unlikely to occur within a completely closed system.

This suggests that the small fractures in diamond in this study play an important role in inclusion modification during decompression (Smith & Nestola, 2021). However, even in the case of small fractures present, it would be incorrect to assume that the system was open to chemical modifications, permitting a constant exchange of material between the inclusion and the diamond-host media. In this case the production of, most likely, low-temperature, and low-pressure epigenetic secondary phases

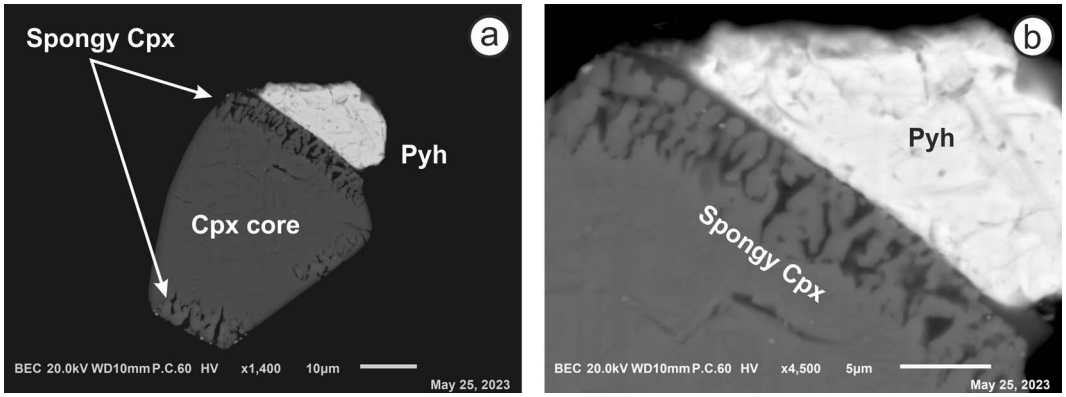

Fig. 8. BSE-images of (a) a touching clinopyroxene and sulfide inclusion in diamond Cln-285 and (b) a close-up of the interface between the spongy-rimmed clinopyroxene and unaltered pyrrhotite (b). Cpx, clinopyroxene; Pyh, Pyrrhotite.

in diamond would be more pronounced. An example of this is the inclusion in Cln-481, which has fully transformed into spongy clinopyroxene and phlogopite. This represents a contrasting case of open system modification, where fluids/melts likely percolated along fractures in the diamond. The presence of phlogopite amongst the secondary products suggests an influx of potassium into the inclusion, providing indirect evidence for the chemically closed system in the other inclusions.

It is important to note that fractures in diamonds often form internally during decompression, without reaching the diamond's exterior. Some examples of such fractures are shown in Figs 1 and 5 in Smith *et al.* (2022); Figs. 01, 5-04, 5-06, 5-16, 5-21 in Tappert & Tappert (2011); Fig. 2 in Smith *et al.* (2014) and Fig. 16D in Taylor & Anand (2004). The latter demonstrates no visible fracture in reflected light and back-scattered electron image, but a strongly visible fracture in cathodoluminescence. In contrast, an example of a fracture that clearly reaches the exterior of the diamond is shown in Supplementary Fig. S15. This figure shows a section of diamond U-345 where a large fracture from the surface has reached a ~10–15-μm mineral inclusion and has caused its complete modification, while a smaller nearby inclusion (~3–5 μm), which was not reached by the fracture, remains intact.

Although most of the diamonds in this study have fractures associated with the spongy-rimmed clinopyroxene inclusions (Fig. 2), we consider that these fractures did not extend to the exterior surface. Therefore, the system remained near-closed, with minimal, if any, exchange with the external environment beyond the host diamond. We find that the presence of a fracture is not a prerequisite for the influx or outflux of a fluid/melt as many clinopyroxenes bound to fractures have not undergone any alteration. For example, in Cln-285 both a spongy-rimmed and pristine clinopyroxene inclusions are connected by the same fracture (Fig. 2b). SEM and EPMA analyses show that the primary clinopyroxene inclusion is homogeneous and does not contain any alteration. The same diamond has a notable additional inclusion: a clinopyroxene with a spongy-rim touching a pyrrhotite (Fig. 8). The spongy texture occurs at the boundary between the clinopyroxene and pyrrhotite as well as on other rims within the grain. However, the sulfide is intact. Although sulfide inclusions in diamond and sulfides in mantle xenoliths are susceptible to metasomatic alteration, there is no evidence of pyrrhotite alteration and the presence of a secondary assemblage including related oxides, hydroxides, or low-pressure and low-temperature sulfides, such as pyrite (Misra *et al.*, 2004; Hughes *et al.*, 2021). Under open-system conditions, it is difficult to imagine a scenario in which only clinopyroxene would be altered by fluid flowing along the grain boundary interface (Fig. 8), while the pyrrhotite remains intact. Moreover, our CT-scan study of two representative inclusions demonstrates that spongy clinopyroxene is mainly concentrated along the crystal edges of the inclusions (3D models provided as Supplementary video files S1 and S2). If the fluid had infiltrated through a fracture into the space between the host diamond and the inclusion, it seems unlikely that it would distribute so uniformly along the edges of the inclusion. Furthermore, some fractures may form in diamonds during their extraction from kimberlites or during polishing to expose inclusions. In this case, inclusions represent zones of weakness, inhomogeneities in the diamond, which may be susceptible to the development of secondary fractures.

Overall, there is strong textural evidence that the studied inclusions are associated with fractures in their diamond hosts, which have likely affected the internal pressure conditions for each inclusion. However, there are no textural signs of any material exchange between the inclusions and the media outside of the diamond.

'Near-closed' system melting: insights into chemical compositions of mineral inclusions

Further evidence in favour of spongy clinopyroxene in diamond having formed in a near-closed system comes from Raman analyses. We observe the presence of the same C–H, C=C and other more complex volatile species in the range of 1400–4500 cm^{-1} in both the primary cores and spongy rims (see chapter 'Raman measurements of volatile phases in core and spongy clinopyroxene' and Fig. 6). If spongy clinopyroxene in our samples formed by processes such as fractional crystallisation or metasomatic fluid-triggered re-crystallisation, we would expect this to differentiate the volatile distribution and element budget between the cores and spongy rims.

Further, we typically do not find additional low-pressure phases occurring with spongy clinopyroxene inclusions, apart from sample Cln-481 (Fig. 1f). In contrast, the occurrence of low-pressure mineral inclusions in diamond (*e.g.*, Fe-oxides, serpentine, amphibole, and hydroxides) indicates extensive interaction with external fluids or melts and the presence of an open system within the diamond (Stachel *et al.*, 2022). Additionally, metasomatic formation (involving external fluid) of the spongy textures observed in mantle eclogitic xenoliths imply the reactions to form new minerals:

Cpx-1 + fluid = Cpx-2 (spongy) + K-Feldspar [1]
(Misra *et al.*, 2004)

Cpx-1 + K-fluid = Cpx-2 (spongy) + Spinel + K-glass ± Plagioclase [2]

(Spetsius & Taylor, 2002)

In the studied inclusions, we observe no reactions leading to the formation of new minerals, except in inclusion Cln-481 that contains phlogopite (Fig. 1f). In contrast, we identified only primary clinopyroxene, residual spongy clinopyroxene and glass (Fig. 1a-e and Supplementary Figs S1–S4).

The most definitive test for the occurrence of near-closed system melting of clinopyroxene in diamond is through mass balance calculations using element compositions of the core, spongy clinopyroxene, and associated glass. However, this approach has its limitations due to the small size of the melt pockets adjacent to spongy clinopyroxene. Inclusion U-530 is the only one with a measured melt composition. The mass balance calculations for this sample have elevated uncertainties due to reliance on EDS measurements, a heterogeneous glass composition, and the lack of a 3D image to correctly assess the proportions of melt.

Nevertheless, using approximately 55–60% melting (determined by the BSE image, Fig. 1e), the mass balance calculations yield discrepancies for all elements below 20% (below 5% for Si, Al and Ca), except for Na which is underestimated by about 30%. Possible reasons for Na-loss are described below.

According to pMELTS calculations, the degree of melting for inclusions in this study ranges between 1 and ~46%, with the majority of primary clinopyroxene inclusions having melted no more than 20–30% (Supplementary Table S3). These calculated values are in good agreement with the area proportions occupied by spongy clinopyroxenes in Fig. 1a–1e and with the 3D tomography data showing that the spongy areas make up 18.6 vol. % of the unexposed and 20.0 vol. % of the exposed clinopyroxene inclusions from diamond U-345 (Supplementary video files S1 and S2).

The very small sizes of individual melt pockets adjacent to spongy clinopyroxene, as confirmed by calculated and measured degrees of melt, make it difficult to obtain the exact melt compositions, even on the scale of mantle xenoliths (Carpenter *et al.*, 2002; Llorens *et al.*, 2019). In the case of tiny inclusions in diamond (~50 μm), the task is more challenging, yielding potentially compromised values. For instance, Taylor *et al.* (2000) list four melt compositions for the W5 inclusion, which vary between 2.80–9.92 wt % MgO and 1.16–5.16 wt % FeO with similar large ranges for other oxides. However, the composition of their partial melt should not be so highly magnesian, due to the highly compatible nature of Mg in clinopyroxene (Hill *et al.*, 2011). This is also supported by the diopside-rich compositions of the spongy clinopyroxenes. Most likely the Mg-rich melt compositions resulted from measurement overlap with the adjacent spongy clinopyroxene, which contains 13 wt % MgO. However, as discussed below in more detail, the melt compositions are likely to also be very heterogeneous.

The lack of reliable melt composition measurements can be substituted by calculated melt compositions modelled by pMELTS. The modelled data shows that partial melting of primary clinopyroxene over a range of P–T conditions can closely reproduce the compositions of spongy clinopyroxenes for all diamond inclusions from this study and Taylor *et al.* (2000) (Supplementary Tables S4–S9). It can also reproduce the glass compositions reasonably well.

Supplementary Tables S4–S9 show measured and calculated spongy clinopyroxene and melt compositions for five diamond inclusions from this study and three diamond inclusions (W1, W5, and W14) from Taylor *et al.* (2000). Regardless of the variations in input parameters, the calculated spongy clinopyroxene compositions demonstrate very little deviation from the measured (within 5–10% for most oxides). A common feature of both measured and modelled melts is their high-alkaline trachytic-phonolitic character, manifested by >50–60 wt % SiO_2, 15–20 wt % Al_2O_3 and ~10 wt % ($Na_2O + K_2O$). However, there are some substantial differences between the modelled melt compositions that relate to the different initial chemical composition of the inclusions (see U-530, W1, W5, W14; Supplementary Tables S4 and S9). pMELTS calculations yield very small amounts of FeO, MgO, CaO in the melt, which does not agree with the measured compositions. We consider this discrepancy to be due to a combination of a pMELTS artefact, analytical challenges, and a high apparent heterogeneity of the melt. The analytical challenges are most likely caused by the overlap with the adjacent pyroxene, or secondary fluorescence during electron microprobe analysis (Jennings *et al.*, 2019).

Interestingly, within the mantle, eclogitic clinopyroxene can melt independently of garnet, resulting in a melt that is not in equilibrium with the bulk rock. This process is common in mantle xenoliths as evidenced by spongy clinopyroxene formed as a product of primary clinopyroxene melting, while kelyphitic rims result from garnet modification. This appears to be possible due to the very high ascent rates of kimberlite magma (days or even hours).

Extraction of potassium and sodium in mantle clinopyroxene by incipient melting

A good proxy for determining a realistic melt composition can be derived from the alkali elements, which are depleted from spongy clinopyroxene during melt extraction; spongy clinopyroxene does not contain K at levels above the detection limit of the electron probe, while its Na concentrations do not exceed 3–4 wt %. However, compared to the measured melt compositions, pMELTS calculations overestimate the Na content of the melts, regardless of the input P–T parameters of melting that we varied substantially. This suggests that an open system influx of Na through any fractures in the diamonds can be ruled out. In contrast, pMELTS underestimates K contents for the melts in inclusions W1, W5, and W14 of Taylor *et al.* (2000) compared to the measured compositions, indicating a potential influx of K. The K content of the melt in inclusion U-530 is very low and agrees with the pMELTS estimates, which is consistent with the low-K concentration in the primary clinopyroxene.

Like Na, K is a highly mobile element and can be easily introduced into the rock and subsequent diamond by a K-bearing fluid (Spetsius & Taylor, 2002). However, as noted by Taylor *et al.* (2000), the concentrations of K in primary clinopyroxene cores of inclusions W1, W5, and W14 are significantly higher than in the clinopyroxene in the diamond-host xenolith. An unlikely scenario to explain this is the introduction of a K-rich fluid into each individual diamond, which then metasomatises the primary clinopyroxene and enriches the melt to the same degree so they both contain 0.6–0.7 wt % K_2O. A more realistic assumption would be that highly potassic primary clinopyroxene in eclogitic diamonds and mantle xenoliths produces K-rich melts. This could be the mechanism for which clinopyroxene within xenoliths is depleted in potassium after one or several melting episodes, while encapsulated inclusions in diamond retain their high potassium concentrations. High potassium contents in eclogitic clinopyroxene inclusions in diamond have been shown to be related to diamond precipitation from saline high-density fluids derived from subduction zones (Izraeli *et al.*, 2001; Izraeli *et al.*, 2004; Weiss *et al.*, 2014; Sverjensky & Huang, 2015; Weiss *et al.*, 2015; Shatskiy

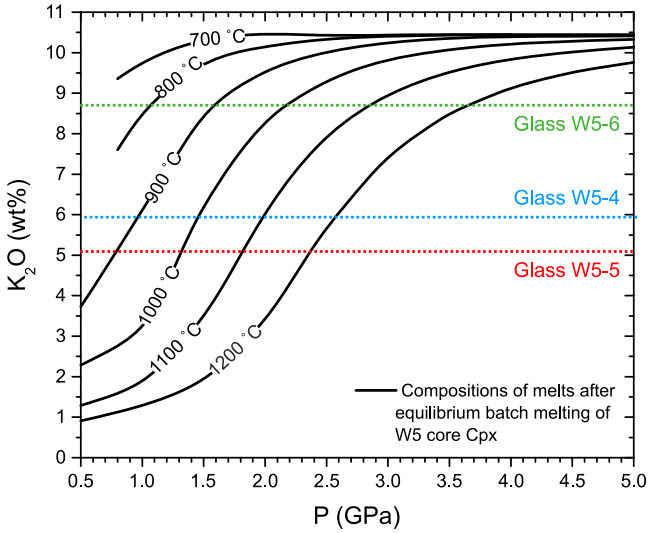

Fig. 9. K_2O compositions of melts modelled by pMELTS for W5 primary clinopyroxene from Taylor *et al.* (2000). Dashed lines indicate the K_2O compositions of glasses for the same inclusion in diamond. The degree of melting (F, in %) decreases progressively from 0.5 to 5.0 GPa for the isotherms as follows: from 69.2 to 6.5 % at 1200°C; from 48.9 to 6.2 % at 1100°C; from 24.6 to 6.1 % at 1000°C; from 15.6 to 6.1 % at 900°C; from 8.3 to 6.0 % at 800°C; and from 6.7 to 6.0 % at 700°C.

et al., 2019; Weiss *et al.*, 2022) as well as high pressures of formation (Harlow, 1997). A lack of high potassium concentration in clinopyroxene in associated xenoliths is suggested to be from subsequent interaction with K_2O undersaturated fluids or melts during the xenoliths mantle storage and evolution (Stachel *et al.*, 2022). In this study, we show an alternative mechanism for potassium removal through the process of melt extraction.

Using the composition of the primary clinopyroxene core from inclusion W5 of Taylor *et al.* (2000), we calculated the K_2O content of the generated melt as a function of pressure along isotherms between 700 and 1200°C (Fig. 9). Our results show that melts formed at low-pressure and low-temperature can readily reproduce the observed K contents. However, high K concentrations in the melt are only feasible at low degrees of melting (<15%). Since the spongy clinopyroxenes in this study exhibit higher degrees of melting (25–43% for inclusion W5), identifying the low temperature conditions in which such melts can form is important.

Spongy clinopyroxene observed as inclusions in diamonds and mantle xenoliths is highly zoned and heterogeneous in composition (Fig. 3). Even on a scale of a few tens of microns, we find variation in Al_2O_3 (3.15–5.45 wt %), and MgO (16.23–18.50 wt %). This can only be explained by the continuous melting of a primary clinopyroxene at a relatively wide range of P–T conditions and a large range in the degrees of melting (Fig. 7). It is difficult to fully explain this style of melting by batch melting as is conducted by pMELTS. Low-degree melts will be highly sodic and potassic, but as melting continues with decreasing pressure, they will gradually become more diluted by the silicate component.

Given that all produced melts are silicic and hence the dihedral angles are high (>60°), melt pockets formed by low degrees of melting may not always be related to the melt formed by higher degrees of melting, causing some melts to be out of equilibrium with the spongy clinopyroxene. This can explain a large variation in melt compositions. Continuous melting also explains the compositional variation observed in spongy clinopyroxenes and can explain various degrees of melting (Figs 1 and 3), while the primary clinopyroxene in the core remains homogeneous in composition.

We consider that the partial melting of clinopyroxene within the diamonds and the resultant formation of spongy clinopyroxene did not occur as a single event. Episodes of melting possibly resulted in the formation of multiple types of melt compositions for different parts of clinopyroxene, even within the same inclusion, as a function of changing P–T conditions (Fig. 3). Various melt compositions in conjunction with compositionally diverse spongy clinopyroxene provide strong evidence for multiple and/or continuous melting events during the diamond's ascent to the surface. This process was probably fast, because the melt did not fractionally crystallise, and although feldspars and spinels are reported (Spetsius & Taylor, 2002) glass is by far the most common phase interstitial to spongy clinopyroxene.

The behaviour of Na is rather enigmatic. pMELTS continuously overestimates the Na content of the melt in comparison with the measured Na concentration of inclusions (U-530, W1, W5, and W14). We suggest a number of explanations for this discrepancy. Firstly, it could result from the loss of water-soluble Na-carbonates that were lost during diamond polishing to expose the inclusion. Alternatively, Na loss from melt pockets may have occurred through any small fractures in the diamond or fluid decrepitation along the fractures. We find it unlikely that Na was the only element to escape the inclusion, as the influx or loss of other oxides, such as K_2O, would also be apparent. However, given the mobility of Na in water-rich fluids and melts (Moore, 2012; Tsay *et al.*, 2017), this cannot be ruled out. Ultimately, in the presence of water, Na is likely to be partitioned into a hydrous silica film, which can be stored at the interface between the diamond and inclusion (Nimis *et al.*, 2016).

Kimberlite ascent to the surface

The thermobarometry for these samples along with the garnet-clinopyroxene thermobarometry reported by Korolev *et al.* (2018b) tells a thorough story of kimberlite magma ascent. The Cullinan samples (Cln-268, -285, and -320) have the most complete P–T history, so we shall discuss them in the most detail, but samples from all three localities are consistent with this overall interpretation (Fig. 10).

The diamonds form at the P–T conditions established by the clinopyroxene-garnet pair (~6 GPa and ~1400°C) (Korolev *et al.*, 2018b). The kimberlite melting is assumed to have last equilibrated with the mantle at the depth of the lithosphere-asthenosphere boundary, which for the Cullinan pipe of the age of 1150 Ma is equivalent to ~210 km (~7 GPa) (Tappe *et al.*, 2018) and a mantle potential temperature of 1375°C (Ganne & Feng, 2017). As the kimberlite ascends, it entrains the diamonds at depths of 180 km (~6 GPa); the diamonds are heated to the temperature of the kimberlite rather quickly. As the magma ascends, the system undergoes decompression causing the formation of fractures within diamonds and triggering the onset of melting of clinopyroxene inclusions. As previously mentioned, we propose multiple episodes of either scenario: the spongy clinopyroxene may have formed through pulses of melting and crystallisation, recording these events, or the primary clinopyroxene may have undergone continuous melting over the range of P–T conditions during kimberlite ascent. However, the rapid nature of this process likely prevented the melts from equilibrating with the surrounding solids. Importantly, the host clinopyroxene melted along the P–T conditions that follow those of the kimberlite. This is seen in the results of our pMELTS modelling and clinopyroxene thermobarometry (Fig. 7), which demonstrate that crystallisation

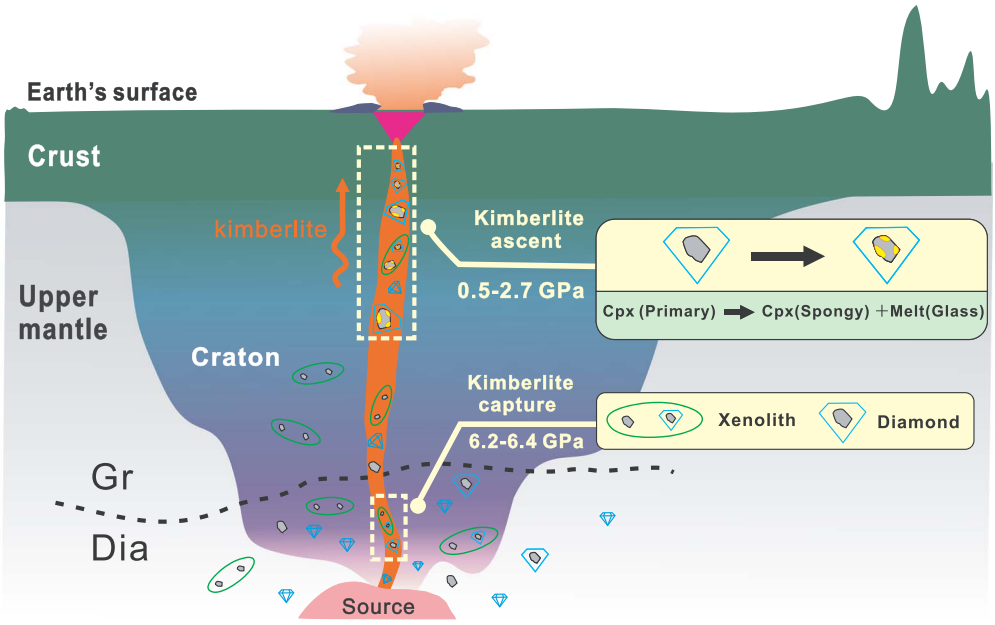

Fig. 10. A model for the formation of spongy clinopyroxene in ascending kimberlite. Using the P–T parameters of sample Cln-320 as an example, the formation process of spongy clinopyroxene during kimberlite ascent is depicted. Kimberlite melt forms at depths within the diamond stability field and ascends, capturing diamonds and mantle xenoliths (the capture pressure of Cln-320 is 6.2–6.4 GPa). For simplicity, only eclogite xenoliths and eclogitic clinopyroxene inclusions in diamonds are considered. During rapid ascent some clinopyroxenes enclosed in diamonds experience partial melting due to decompression, leading to the formation of a spongy rim and melt (the decompression melting range of Cln-320 is 0.5–2.7 GPa). The studied clinopyroxene inclusions preserve the decompression record that led to the formation of spongy clinopyroxene and melt. The orange arrow indicates the ascent direction of the kimberlite magma. Cpx, clinopyroxene; Gr, graphite; Dia, diamond.

temperature and pressure are correlated along a decompression path. These estimates also generally agree with the kimberlite P–T ascent paths calculated by Kavanagh & Sparks (2009) for a mantle potential temperature of 1375 ± 40°C (Ganne & Feng, 2017).

CONCLUSIONS

1) We studied six eclogitic clinopyroxene inclusions in six diamonds. Five of the inclusions contain primary clinopyroxene cores and spongy clinopyroxene rims. The sixth inclusion contains spongy clinopyroxene with phlogopite. The latter serves as an example of formation in an open system. The following conclusions apply to the five studied inclusions, which formed in a closed or nearly closed system.
2) Each inclusion provides a snapshot of its melting history, allowing us to reconstruct the formation of spongy clinopyroxene within the host diamond. Unlike mantle xenoliths, modified by superimposed processes (metasomatism, partial melting, re-crystallisation, interaction with kimberlite melts, etc.), mineral inclusions in diamonds provide a unique opportunity to examine clinopyroxene melting without the influence of external fluids or melts. Instead, we argue that its formation occurred due to decompression melting. Given that the vast majority of eclogitic and peridotitic mantle xenoliths transported to the surface by kimberlites contain spongy clinopyroxene, this process is likely a common mechanism for modifying primary xenolith assemblages associated with kimberlite magmatism.
3) Textural features, major element compositions, thermobarometry and geochemical modelling (pMELTS) establish that the primary clinopyroxene was captured within the diamond stability field and underwent partial melting inside the host diamond at pressures below 2.7 GPa. These pressures are lower than diamond (or xenolith containing diamond) entrapment by the kimberlite melt. As the kimberlite carried the diamonds to the surface, the combined effects of high temperatures and decompression triggered the melting of clinopyroxene inclusions, leading to the crystallisation of spongy clinopyroxene.
4) We consider that the system was near-closed, with no chemical exchange with the external environment, but subject to internal changes in pressure and temperature. Evidence supporting incipient melting of primary clinopyroxene within the diamond after inclusion entrapment includes: identical Raman spectra between the primary cores and spongy rims, indicating similar compound composition (Raman bands); compositional variations in spongy clinopyroxene within the same grain; the localisation of spongy clinopyroxene exclusively along crystal edges, in contrast to mantle xenoliths, where spongy textures completely surround grains due to fluid infiltration; refractory diopside compositions compared to the enriched primary omphacite; and formation at low pressures and temperatures (<2.7 GPa; pMELTS modelling and Putirka (2008) barometer).
5) The major-element compositions of spongy clinopyroxene and the associated melt vary significantly on a micro-scale across different parts of inclusion rims. However, there is no systematic zoning or pattern to the chemical variations in the spongy clinopyroxene compositions. We suggest these results either from multiple pulses of melting across a wide range of pressures (0.5–2.7 GPa) upon the diamond's journey to the surface, or from a lack of melt-solid equilibrium due to the rapid ascent to the surface.
6) Established P–T conditions for spongy clinopyroxene formation allow for the reconstruction of a P–T path for kimberlite ascent, which is in a good agreement with previous models.

SUPPLEMENTARY DATA

Supplementary data are available at *Journal of Petrology* online.

ACKNOWLEDGEMENTS

We thank the Editor Carl Spandler for his editorial handling and the two anonymous reviewers for their extensive and thorough reviews, which significantly contributed to improving the manuscript. We acknowledge support from IRC grant IRCLA/2022/2638 to E.S.K., the Kalbfleisch Fellowship to N.M.K., and RSF 21-77-20026 grant to E.V. N.M.K acknowledges the support from the Richard Gilder Graduate School, American Museum of Natural History E.S.K thanks U.S. National Science Foundation (NSF) award 2320473 from the Major Research Instrumentation (MRI) program. We thank Lyudmila I. Luk'yanova and Igor Klepikov for their assistance in the Ural sample selection and preparation for the study.

DATA AVAILABILITY

The data described and used in this article are available in the text, online supplementary material, and have been published via GFZ Data Services with the DOI https://doi.org/10.5880/fidgeo.2025.027 (Wang *et al.*, 2025).

REFERENCES

Abersteiner, A., Kamenetsky, V. S., Goemann, K., Golovin, A. V., Sharygin, I. S., Pearson, D. G., Kamenetsky, M. & Gornova, M. A. (2019). Polymineralic inclusions in kimberlite-hosted megacrysts: implications for kimberlite melt evolution. *Lithos* **336-337**, 310–325. https://doi.org/10.1016/j.lithos.2019.04.004.

Aulbach, S., Woodland, A. B., Vasilyev, P., Galvez, M. E. & Viljoen, K. S. (2017). Effects of low-pressure igneous processes and subduction on Fe3+/ΣFe and redox state of mantle eclogites from lace (Kaapvaal craton). *Earth and Planetary Science Letters* **474**, 283–295. https://doi.org/10.1016/j.epsl.2017.06.030.

Barron, L. M. (2005). A linear model and topology for the host–inclusion mineral system involving diamond. *The Canadian Mineralogist* **43**, 203–224. https://doi.org/10.2113/gscanmin.43.1.203.

Barth, M. G., Rudnick, R. L., Horn, I., McDonough, W. F., Spicuzza, M. J., Valley, J. W. & Haggerty, S. E. (2002). Geochemistry of xenolithic eclogites from West Africa, part 2: origins of the high MgO eclogites. *Geochimica et Cosmochimica Acta* **66**, 4325–4345. https://doi.org/10.1016/S0016-7037(02)01004-9.

Beard, B. L., Fraracci, K. N., Taylor, L. A., Snyder, G. A., Clayton, R. A., Mayeda, T. K. & Sobolev, N. V. (1996). Petrography and geochemistry of eclogites from the Mir kimberlite, Yakutia, Russia. *Contributions to Mineralogy and Petrology* **125**, 293–310. https://doi.org/10.1007/s004100050223.

Blundy, J. D., Falloon, T. J., Wood, B. J. & Dalton, J. A. (1995). Sodium partitioning between clinopyroxene and silicate melts. *Journal of Geophysical Research-Solid Earth* **100**, 15501–15515. https://doi.org/10.1029/95JB00954.

Bruno, M., Ghignone, S., Aquilano, D., & Nestola, F. (2024). A critique of using epitaxial criterion to discriminate between protogenetic and syngenetic mineral inclusions in diamond. *Scientific Reports* **14**(1), 8674. https://doi.org/10.1038/s41598-024-59432-6.

Burness, S., Smart, K. A., Tappe, S., Stevens, G., Woodland, A. B. & Cano, E. (2020). Sulphur-rich mantle metasomatism of Kaapvaal craton eclogites and its role in redox-controlled platinum group element mobility. *Chemical Geology* **542**, 119476. https://doi.org/10.1016/j.chemgeo.2020.119476.

Bussweiler, Y., Stone, R. S., Pearson, D. G., Luth, R. W., Stachel, T., Kjarsgaard, B. A. & Menzies, A. (2016). The evolution of calcite-bearing kimberlites by melt-rock reaction: evidence from polymineralic inclusions within clinopyroxene and garnet megacrysts from lac de Gras kimberlites, Canada. *Contributions to Mineralogy and Petrology* **171**, 65. https://doi.org/10.1007/s00410-016-1275-3.

Caporuscio, F. A. & Smyth, J. R. (1990). Trace element crystal chemistry of mantle eclogites. *Contributions to Mineralogy and Petrology* **105**, 550–561. https://doi.org/10.1007/BF00302494.

Carpenter, R. L., Edgar, A. D. & Thibault, Y. (2002). Origin of spongy textures in clinopyroxene and spinel from mantle xenoliths, hessian depression, Germany. *Mineralogy and Petrology* **74**, 149–162. https://doi.org/10.1007/s007100200002.

Chien, Y.-H., Wang, K.-L., Kovach, V., Kuzmin, M., Vorontsov, A., Ivanov, A., Pang, K.-N., Iizuka, Y., Lee, H.-Y., Chung, S.-L. & Lee, D. C. (2024). Geochemical characteristics of peridotite xenoliths from the Vitim volcanic field: insight to late Cenozoic mantle upwelling in SE Siberia. *Lithos* **482-483**, 107727. https://doi.org/10.1016/j.lithos.2024.107727.

Czas, J., Stachel, T., Pearson, D. G., Stern, R. A., & Read, G. H. (2018). Diamond brecciation and annealing accompanying major metasomatism in eclogite xenoliths from the Sask Craton, Canada. *Mineralogy and Petrology* **112**(S1), 311–323. https://doi.org/10.1007/s00710-018-0590-y.

Day, H. W. (2012). A revised diamond-graphite transition curve. *American Mineralogist* **97**(1), 52–62. https://doi.org/10.2138/am.2011.3763.

De Hoog, J. C. M., Gall, L. & Cornell, D. H. (2010). Trace-element geochemistry of mantle olivine and application to mantle petrogenesis and geothermobarometry. *Chemical Geology* **270**, 196–215. https://doi.org/10.1016/j.chemgeo.2009.11.017.

De Stefano, A., Kopylova, M. G., Cartigny, P. & Afanasiev, V. (2009). Diamonds and eclogites of the Jericho kimberlite (northern Canada). *Contributions to Mineralogy and Petrology* **158**, 295–315. https://doi.org/10.1007/s00410-009-0384-7.

Dludla, S., le Roex, A. P. & Gurney, J. J. (2006). Eclogite xenoliths from the premier kimberlite, South Africa: geochemical evidence for a subduction origin. *South African Journal of Geology* **109**, 353–368. https://doi.org/10.2113/gssajg.109.3.353.

Eremets, M. I., Popov, M. Y., Trojan, I. A., Denisov, V. N., Boehler, R. & Hemley, R. J. (2004). Polymerization of nitrogen in sodium azide. *The Journal of Chemical Physics* **120**, 10618–10623. https://doi.org/10.1063/1.1718250.

Fung, A. T. & Haggerty, S. E. (1995). Petrography and mineral compositions of eclogites from the Koidu kimberlite complex, sierra-Leone. *Journal of Geophysical Research-Solid Earth* **100**, 20451–20473. https://doi.org/10.1029/95JB01573.

Ganne, J. & Feng, X. (2017). Primary magmas and mantle temperatures through time. *Geochemistry, Geophysics, Geosystems* **18**, 872–888. https://doi.org/10.1002/2016GC006787.

Ghiorso, M. S., Hirschmann, M. M., Reiners, P. W. & Kress, V. C. (2002). The pMELTS: a revision of MELTS for improved calculation of phase relations and major element partitioning related to partial melting of the mantle to 3 GPa. *Geochemistry, Geophysics, Geosystems* **3**, 1–35. https://doi.org/10.1029/2001GC000217.

Grahanov, S., Shatalov, V. & Shtyrov, V. (2007). Diamond placers of Russia. *Novosibirsk: Geo* **457**.

Griffin, W., Wass, S. & Hollis, J. (1984). Ultramafic xenoliths from Bullenmerri and Gnotuk maars, Victoria, Australia: petrology of a sub-continental crust-mantle transition. *Journal of Petrology* **25**, 53–87. https://doi.org/10.1093/petrology/25.1.53.

Gualda, G. A. & Ghiorso, M. S. (2015). MELTS _ E xcel: AM icrosoft E xcel-based MELTS interface for research and teaching of magma properties and evolution. *Geochemistry, Geophysics, Geosystems* **16**, 315–324. https://doi.org/10.1002/2014GC005545.

Harlow, G. E. (1997). K in clinopyroxene at high pressure and temperature: an experimental study. *American Mineralogist* **82**, 259–269. https://doi.org/10.2138/am-1997-3-403.

Harte, B. & Cayzer, N. (2007). Decompression and unmixing of crystals included in diamonds from the mantle transition zone. *Physics and Chemistry of Minerals* **34**, 647–656. https://doi.org/10.1007/s00269-007-0178-2.

Hasterok, D., & Chapman, D. S. (2011). Heat production and geotherms for the continental lithosphere. *Earth and Planetary Science Letters* **307**(1-2), 59–70. https://doi.org/10.1016/j.epsl.2011.04.034.

Hill, E., Blundy, J. D. & Wood, B. J. (2011). Clinopyroxene-melt trace element partitioning and the development of a predictive model for HFSE and Sc. *Contributions to Mineralogy and Petrology* **161**, 423–438. https://doi.org/10.1007/s00410-010-0540-0.

Huang, J. X., Greau, Y., Griffin, W. L., O'Reilly, S. Y. & Pearson, N. J. (2012). Multi-stage origin of Roberts victor eclogites: progressive metasomatism and its isotopic effects. *Lithos* **142-143**, 161–181. https://doi.org/10.1016/j.lithos.2012.03.002.

Huang, J.-X., Griffin, W. L., Gréau, Y., Pearson, N. J., O'Reilly, S. Y., Cliff, J. & Martin, L. (2014). Unmasking xenolithic eclogites: progressive metasomatism of a key Roberts victor sample. *Chemical Geology* **364**, 56–65. https://doi.org/10.1016/j.chemgeo.2013.11.025.

Hughes, H. S. R., Compton-Jones, C., McDonald, I., Kiseeva, E. S., Kamenetsky, V. S., Rollinson, G., Coggon, J. A., Kinnaird, J. A. & Bybee, G. M. (2021). Base metal sulphide geochemistry of southern African mantle eclogites (Roberts victor): implications for cratonic mafic magmatism and metallogenesis. *Lithos* **382-383**, 105918. https://doi.org/10.1016/j.lithos.2020.105918.

Ionov, D. A., Hofmann, A. W. & Shimizu, N. (1994). Metasomatism-induced melting in mantle xenoliths from Mongolia. *Journal of Petrology* **35**, 753–785. https://doi.org/10.1093/petrology/35.3.753.

Izraeli, E. S., Harris, J. W. & Navon, O. (2001). Brine inclusions in diamonds: a new upper mantle fluid. *Earth and Planetary Science Letters* **187**, 323–332. https://doi.org/10.1016/S0012-821X(01)00291-6.

Izraeli, E. S., Harris, J. W. & Navon, O. (2004). Fluid and mineral inclusions in cloudy diamonds from Koffiefontein, South Africa. *Geochimica et Cosmochimica Acta* **68**, 2561–2575. https://doi.org/10.1016/j.gca.2003.09.005.

Jennings, E. S. & Holland, T. J. (2015). A simple thermodynamic model for melting of peridotite in the system NCFMASOCr. *Journal of Petrology* **56**, 869–892. https://doi.org/10.1093/petrology/egv020.

Jennings, E. S., Wade, J., Laurenz, V. & Petitgirard, S. (2019). Diamond anvil cell partitioning experiments for accretion and core formation: testing the limitations of electron microprobe analysis. *Microscopy and Microanalysis* **25**, 1–10. https://doi.org/10.1017/S1431927618015568.

Jorgenson, C., Higgins, O., Petrelli, M., Bégué, F. & Caricchi, L. (2022). A machine learning-based approach to clinopyroxene thermobarometry: model optimization and distribution for use in earth sciences. *Journal of Geophysical Research: Solid Earth* **127**, e2021JB022904. https://doi.org/10.1029/2021JB022904.

Kargin, A. V., Sazonova, L. V., Nosova, A. A., & Tretyachenko, V. V. (2016). Composition of garnet and clinopyroxene in peridotite xenoliths from the Grib kimberlite pipe, Arkhangelsk diamond province, Russia: Evidence for mantle metasomatism associated with kimberlite melts. *Lithos*, **262**, 442-455. https://doi.org/10.1016/j.lithos.2016.07.015.

Kargin, A., Sazonova, L., Nosova, A., Lebedeva, N., Tretyachenko, V. & Abersteiner, A. (2017). Cr-rich clinopyroxene megacrysts from the Grib kimberlite, Arkhangelsk province, Russia: relation to clinopyroxene–phlogopite xenoliths and evidence for mantle metasomatism by kimberlite melts. *Lithos* **292-293**, 34–48. https://doi.org/10.1016/j.lithos.2017.08.018.

Katsura, T., Yoneda, A., Yamazaki, D., Yoshino, T., & Ito, E. (2010). Adiabatic temperature profile in the mantle. *Physics of the Earth and Planetary Interiors* **183**(1-2), 212–218. https://doi.org/10.1016/j.pepi.2010.07.001.

Kavanagh, J. L. & Sparks, R. S. J. (2009). Temperature changes in ascending kimberlite magma. *Earth and Planetary Science Letters* **286**, 404–413. https://doi.org/10.1016/j.epsl.2009.07.011.

Khachatryan, G., Zinchuk, N., Koptil, V., Gurkina, G. & Kharrasov, M. (2004). Study of optically active centers in diamonds from Uralian placers: an attempt to locate their primary deposits. *Russian Geology and Geophysics* **45**, 244–252.

Kiseeva, E. S., Kamenetsky, V. S., Yaxley, G. M. & Shee, S. R. (2017). Mantle melting versus mantle metasomatism - "the chicken or the egg" dilemma. *Chemical Geology* **455**, 120–130. https://doi.org/10.1016/j.chemgeo.2016.10.026.

Knippers, W., Van Helvoort, K., De Felici, M., Reuss, J. & Stolte, S. (1986). The allene Raman spectrum from 250 to 6200 cm−1 stokes shift. *Chemical Physics* **105**, 27–39. https://doi.org/10.1016/0301-0104(86)80053-2.

Kolesnikov, A., Kutcherov, V. G. & Goncharov, A. F. (2009). Methane-derived hydrocarbons produced under upper-mantle conditions. *Nature Geoscience* **2**, 566–570. https://doi.org/10.1038/ngeo591.

Kopylova, M., Tso, E., Ma, F., Liu, J. & Pearson, D. (2019). The metasomatized mantle beneath the North Atlantic craton: insights from peridotite xenoliths of the Chidliak kimberlite province (NE Canada). *Journal of Petrology* **60**, 1991–2024. https://doi.org/10.1093/petrology/egz061.

Korolev, N., Kopylova, M., Gurney, J. J., Moore, A. E. & Davidson, J. (2018a). The origin of type II diamonds as inferred from Cullinan mineral inclusions. *Mineralogy and Petrology.* **112**, 275–289. https://doi.org/10.1007/s00710-018-0601-z.

Korolev, N. M., Kopylova, M., Bussweiler, Y., Pearson, D. G., Gurney, J. & Davidson, J. (2018b). The uniquely high-temperature character of Cullinan diamonds: a signature of the Bushveld mantle plume? *Lithos* **304**, 362–373. https://doi.org/10.1016/j.lithos.2018.02.011.

Korolev, N., Nikitina, L. P., Goncharov, A., Dubinina, E. O., Melnik, A., Müller, D., Chen, Y.-X. & Zinchenko, V. N. (2021). Three types of mantle eclogite from two layers of oceanic crust: a key case of metasomatically-aided transformation of low-to-high-magnesian eclogite. *Journal of Petrology* **62**, egab070. https://doi.org/10.1093/petrology/egab070.

Korolev, N., Kopylova, M., Dubinina, E. & Stern, R. (2023). Contrasting oxygen isotopes in garnet from diamondiferous and barren eclogitic parageneses. *Geochemical Perspectives Letters* **27**, 15–19. https://doi.org/10.7185/geochemlet.2328.

Lebedeva, N. M., Nosova, A. A., Sazonova, L. V. & Larionova, Y. O. (2022). Metasomatized xenoliths of mantle eclogites and garnet pyroxenites from the V. Grib kimberlite, Arkhangelsk Province. *Petrology* **30**, 479–498. https://doi.org/10.1134/S0869591122050046.

Liu, Y., Taylor, L. A., Sarbadhikari, A. B., Valley, J. W., Ushikubo, T., Spicuzza, M. J., Kita, N., Ketcham, R. A., Carlson, W., Shatsky, V. & Sobolev, N. V. (2009). Metasomatic origin of diamonds in the world's largest diamondiferous eclogite. *Lithos* **112**(2), 1014–1024. https://doi.org/10.1016/j.lithos.2009.06.036.

Llorens, M.-G., Gomez-Rivas, E., Ganzhorn, A.-C., Griera, A., Steinbach, F., Roessiger, J., Labrousse, L., Walte, N. P., Weikusat, I. & Bons, P. D. (2019). The effect of dynamic recrystallisation

on the rheology and microstructures of partially molten rocks. *Journal of Structural Geology* **118**, 224–235. https://doi.org/10.1016/j.jsg.2018.10.013.

Lu, J., Zheng, J., Griffin, W. L., O'Reilly, S. Y. & Pearson, N. J. (2015). Microscale effects of melt infiltration into the lithospheric mantle: peridotite xenoliths from Xilong, South China. *Lithos* **232**, 111–123. https://doi.org/10.1016/j.lithos.2015.06.013.

Ma, G. S. K., Wang, K.-L., Malpas, J., Iizuka, Y., Xenophontos, C., Turkmani, A. A., Chan, G. H. N., Usuki, T. & Chan, Q. H. S. (2015) Melt pockets and spongy clinopyroxenes in mantle xenoliths from the Plio-Quaternary Al Ghab Volcanic Field, NW Syria: implications for the metasomatic evolution of the lithosphere. In: Khan A. & Deschamps F. (eds) *The Earth's Heterogeneous Mantle: A Geophysical, Geodynamical, and Geochemical Perspective*. Cham: Springer International Publishing, pp.205–257.

Menzies, M., Kempton, P. & Dungan, M. (1985). Interaction of continental lithosphere and asthenospheric melts below the Geronimo volcanic field, Arizona, USA. *Journal of Petrology* **26**, 663–693. https://doi.org/10.1093/petrology/26.3.663.

Misra, K. C., Anand, M., Taylor, L. A. & Sobolev, N. V. (2004). Multistage metasomatism of diamondiferous eclogite xenoliths from the Udachnaya kimberlite pipe, Yakutia, Siberia. *Contributions to Mineralogy and Petrology* **146**, 696–714. https://doi.org/10.1007/s00410-003-0529-z.

Moore, K. R. (2012). Experimental study in the Na2O-CaO-MgO-Al2O3-SiO2-CO2 system at 3 GPa: the effect of sodium on mantle melting to carbonate-rich liquids and implications for the petrogenesis of silicocarbonatites. *Mineralogical Magazine* **76**, 285–309. https://doi.org/10.1180/minmag.2012.076.2.04.

Morimoto, N., Fabries, J., Ferguson, A. K., Ginzburg, I.V., Ross, M., Seifert, F.A., Zussman, J., Aoki, K. & Gottardi, G. (1988). Nomenclature of pyroxenes. *American Mineralogist* **73**, 1123–1133.

Müller, T., Dohmen, R., Becker, H. W., ter Heege, J. H., & Chakraborty, S. (2013). Fe–Mg interdiffusion rates in clinopyroxene: experimental data and implications for Fe–Mg exchange geothermometers. *Contributions to Mineralogy and Petrology* **166**(6), 1563–1576. https://doi.org/10.1007/s00410-013-0941-y.

Neave, D. A. & Putirka, K. D. (2017). A new clinopyroxene-liquid barometer, and implications for magma storage pressures under Icelandic rift zones. *American Mineralogist* **102**, 777–794. https://doi.org/10.2138/am-2017-5968.

Nestola, F., Nimis, P., Ziberna, L., Longo, M., Marzoli, A., Harris, J. W., Manghnani, M. H. & Fedortchouk, Y. (2011). First crystal-structure determination of olivine in diamond: composition and implications for provenance in the Earth's mantle. *Earth and Planetary Science Letters* **305**, 249–255. https://doi.org/10.1016/j.epsl.2011.03.007.

Nestola, F., Regier, M. E., Luth, R. W., Pearson, D. G., Stachel, T., McCammon, C., Wenz, M. D., Jacobsen, S. D., Anzolini, C., Bindi, L. & Harris, J. W. (2023). Extreme redox variations in a superdeep diamond from a subducted slab. *Nature* **613**, 85–89. https://doi.org/10.1038/s41586-022-05392-8.

Nikulin, I. I. (2022). Retrospective Mineragenic analysis of deposits of the Vishera diamond-bearing zone (eastern margin of the Russian platform). *Geology of Ore Deposits* **64**, 43–59. https://doi.org/10.1134/S1075701522090069.

Nimis, P., Alvaro, M., Nestola, F., Angel, R. J., Marquardt, K., Rustioni, G., Harris, J. W. & Marone, F. (2016). First evidence of hydrous silicic fluid films around solid inclusions in gem-quality diamonds. *Lithos* **260**, 384–389. https://doi.org/10.1016/j.lithos.2016.05.019.

Otto, T., Stevens, G., Mayne, M. J. & Moyen, J.-F. (2023). Phase equilibrium modelling of partial melting in the upper mantle: a comparison between different modelling methodologies and experimental results. *Lithos* **444-445**, 107111. https://doi.org/10.1016/j.lithos.2023.107111.

Pan, S., Zheng, J., Yin, Z., Griffin, W., Xia, M., Lin, A. & Zhang, H. (2018). Spongy texture in mantle clinopyroxene recordsdecompression-induced melting. *Lithos* **320-321**, 144–154. https://doi.org/10.1016/j.lithos.2018.08.035.

Pobric, V., Korolev, N. & Kopylova, M. (2020). Eclogites of the North Atlantic craton: insights from the Chidliak eclogite xenoliths (S. Baffin Island, Canada). *Contributions to Mineralogy and Petrology* **175**, 71. https://doi.org/10.1007/s00410-020-01709-w.

Putirka, K. D. (2008). Thermometers and barometers for volcanic systems. *Minerals, Inclusions and Volcanic Processes* **69**, 61–120. https://doi.org/10.1515/9781501508486-004.

Pyle, J. M. & Haggerty, S. E. (1998). Eclogites and the metasomatism of eclogites from the Jagersfontein kimberlite: punctuated transport and implications for alkali magmatism. *Geochimica et Cosmochimica Acta* **62**, 1207–1231. https://doi.org/10.1016/S0016-7037(98)00040-4.

Rakin, V. I. (2013). Morphology of Ural-type diamonds. *Yekaterinburg: UrB RAS*(in Russian) . https://doi.org/10.19110/7691-026.

Sampathkumar, K., Diez-Cabanes, V., Kovaricek, P., del Corro, E., Bouša, M., Hošek, J., Kalbac, M. & Frank, O. (2019). On the suitability of Raman spectroscopy to monitor the degree of graphene functionalization by Diazonium salts. *The Journal of Physical Chemistry C* **123**, 22397–22402. https://doi.org/10.1021/acs.jpcc.9b06516.

Schiano, P. & Clocchiatti, R. (1994). Worldwide occurrence of silica-rich melts in sub-continental and sub-oceanic mantle minerals. *Nature* **368**, 621–624. https://doi.org/10.1038/368621a0.

Schiano, P., Clocchiatti, R., Shimizu, N., Weis, D. & Mattielli, N. (1994). Cogenetic silica-rich and carbonate-rich melts trapped in mantle minerals in Kerguelen ultramafic xenoliths: implications for metasomatism in the oceanic upper mantle. *Earth and Planetary Science Letters* **123**, 167–178. https://doi.org/10.1016/0012-821X(94)90265-8.

Shatskiy, A., Arefiev, A. V., Podborodnikov, I. V. & Litasov, K. D. (2019). Origin of K-rich diamond-forming immiscible melts and CO2 fluid via partial melting of carbonated pelites at a depth of 180–200 km. *Gondwana Research* **75**, 154–171. https://doi.org/10.1016/j.gr.2019.05.004.

Smart, K. A., Tappe, S., Woodland, A. B., Greyling, D. R., Harris, C. & Gussone, N. (2021). Constraints on Archean crust recycling and the origin of mantle redox variability from the δ44/40Ca–δ18O–fO2 signatures of cratonic eclogites. *Earth and Planetary Science Letters* **556**, 116720. https://doi.org/10.1016/j.epsl.2020.116720.

Smith, E. M. & Nestola, F. (2021). Super-deep diamonds. *Mantle Convection and Surface Expressions* , 179–192. https://doi.org/10.1002/9781119528609.ch7.

Smith, E. M., Kopylova, M. G., Frezzotti, M. L. & Afanasiev, V. P. (2014). N-rich fluid inclusions in octahedrally-grown diamond. *Earth and Planetary Science Letters* **393**, 39–48. https://doi.org/10.1016/j.epsl.2014.02.033.

Smith, E. M., Krebs, M. Y., Genzel, P.-T. & Brenker, F. E. (2022). Raman identification of inclusions in diamond. *Reviews in Mineralogy and Geochemistry* **88**, 451–473. https://doi.org/10.2138/rmg.2022.88.08.

Sobolev, V. N., Taylor, L. A., Snyder, G. A., Jerde, E. A., Neal, C. R. & Sobolev, N. V. (1999). Quantifying the effects of metasomatism in mantle xenoliths: constraints from secondary chemistry and mineralogy in Udachnaya eclogites, Yakutia. *International Geology Review* **41**, 391–416. https://doi.org/10.1080/00206819909465149.

Sobolev, N., Logvinova, A. & Efimova, E. (2009). Syngenetic phlogopite inclusions in kimberlite-hosted diamonds: implications for role

of volatiles in diamond formation. *Russian Geology and Geophysics* **50**, 1234–1248. https://doi.org/10.1016/j.rgg.2009.11.021.

Sobolev, N. V., Logvinova, A. M., Tomilenko, A. A., Wirth, R., Bul'bak, T. A., Luk'yanova, L. I., Fedorova, E. N., Reutsky, V. N. & Efimova, E. S. (2019). Mineral and fluid inclusions in diamonds from the Urals placers, Russia: evidence for solid molecular N2 and hydrocarbons in fluid inclusions. *Geochimica et Cosmochimica Acta* **266**, 197–219. https://doi.org/10.1016/j.gca.2019.08.028.

Socrates, G. (2004) *Infrared and Raman characteristic group frequencies: tables and charts*, 3rd edn. Chichester, West Sussex: John Wiley & Sons, Ltd.

Solin, S. A., & Ramdas, A. K. (1970). Raman Spectrum of Diamond. *Physical Review B* **1**(4), 1687–1698. https://doi.org/10.1103/physrevb.1.1687.

Somayazulu, M. S., Finger, L. W., Hemley, R. J. & K., M. H. (1996). High-pressure compounds in methane-hydrogen mixtures. *Science* **271**, 1400–1402. https://doi.org/10.1126/science.271.5254.1400.

Spetsius, Z. & Taylor, L. (2002). Partial melting in mantle eclogite xenoliths: connections with diamond paragenesis. *International Geology Review* **44**, 973–987. https://doi.org/10.2747/0020-6814.44.11.973.

Stachel, T. & Harris, J. W. (2008). The origin of cratonic diamonds - constraints from mineral inclusions. *Ore Geology Reviews* **34**, 5–32. https://doi.org/10.1016/j.oregeorev.2007.05.002.

Stachel, T., Aulbach, S. & Harris, J. W. (2022). Mineral inclusions in lithospheric diamonds. *Reviews in Mineralogy and Geochemistry* **88**, 307–391. https://doi.org/10.2138/rmg.2022.88.06.

Su, B. X., Zhang, H. F., Sakyi, P. A., Yang, Y. H., Ying, J. F., Tang, Y. J., Qin, K. Z., Xiao, Y., Zhao, X. M., Mao, Q. A. & Ma, Y. G. (2011). The origin of spongy texture in minerals of mantle xenoliths from the Western Qinling, Central China. *Contributions to Mineralogy and Petrology* **161**, 465–482. https://doi.org/10.1007/s00410-010-0543-x.

Sverjensky, D. A. & Huang, F. (2015). Diamond formation due to a pH drop during fluid-rock interactions. *Nature Communications* **6**. https://doi.org/10.1038/ncomms9702.

Tappe, S., Smart, K., Torsvik, T., Massuyeau, M. & de Wit, M. (2018). Geodynamics of kimberlites on a cooling earth: clues to plate tectonic evolution and deep volatile cycles. *Earth and Planetary Science Letters* **484**, 1–14. https://doi.org/10.1016/j.epsl.2017.12.013.

Tappert, R. & Tappert, M. C. (2011). Diamonds in nature: a guide to rough diamonds. *Diamonds in Nature: A Guide to Rough Diamonds* , 1–142.

Taylor, L. A. & Anand, M. (2004). Diamonds: time capsules from the Siberian mantle. *Chemie der Erde-Geochemistry* **64**, 1–74. https://doi.org/10.1016/j.chemer.2003.11.006.

Taylor, L. A. & Neal, C. R. (1989). Eclogites with oceanic crustal and mantle signatures from the Bellsbank kimberlite, South-Africa, part 1: mineralogy, petrography, and whole rock chemistry. *Journal of Geology* **97**, 551–567. https://doi.org/10.1086/629334.

Taylor, L. A., Keller, R. A., Snyder, G. A., Wang, W. Y., Carlson, W. D., Hauri, E. H., McCandless, T., Kim, K. R., Sobolev, N. V. & Bezborodov, S. M. (2000). Diamonds and their mineral inclusions, and what they tell us: a detailed "pull-apart" of a diamondiferous eclogite. *International Geology Review* **42**, 959–983. https://doi.org/10.1080/00206810009465120.

Tsay, A., Zajacz, Z., Ulmer, P. & Sanchez-Valle, C. (2017). Mobility of major and trace elements in the eclogite-fluid system and element fluxes upon slab dehydration. *Geochimica et Cosmochimica Acta* **198**, 70–91. https://doi.org/10.1016/j.gca.2016.10.038.

Vasilev, E., Klepikov, I. & Lukianova, L. (2019). Comparison of diamonds from the Rassolninskaya depression and modern alluvial placers of the Krasnovishersky district (Ural region). *Geology of Ore Deposits* **61**, 598–605. https://doi.org/10.1134/S1075701519070134.

Viljoen, F., Dobbe, R. & Smit, B. (2009). Geochemical processes in peridotite xenoliths from the premier diamond mine, South Africa: evidence for the depletion and refertilisation of subcratonic lithosphere. *Lithos* **112**, 1133–1142. https://doi.org/10.1016/j.lithos.2009.05.004.

Wang, C., Guo, P., Xiong, S., Wang, F. & Xu, W. (2024). Two styles of melt-peridotite interactions in the upper mantle revealed by mantle xenoliths from northeastern China. *Lithos* **468-469**, 107485. https://doi.org/10.1016/j.lithos.2023.107485.

Wang, W., Korolev, N. M., Kiseeva, E. S., Davies, R. M., Weiss, Y., Kopylova, M., Towbin, W. H., Huang, F., Moore, A. E. & Vasilev, E. A. (2025) *Analytical, modelled, and imaging data of eclogitic clinopyroxene inclusions hosted in diamonds from the Cullinan Mine (South Africa) and the Rassolnaya Placer (Urals Mountains, Russia)*. GFZ Data Services. GFZ Helmholtz Centre for Geosciences, Potsdam, Germany. https://doi.org/10.5880/fidgeo.2025.027.

Warr, L. N. (2021). IMA–CNMNC approved mineral symbols. *Mineralogical Magazine* **85**(3), 291–320. https://doi.org/10.1180/mgm.2021.43.

Weiss, Y., Kiflawi, I., Davies, N. & Navon, O. (2014). High-density fluids and the growth of monocrystalline diamonds. *Geochimica et Cosmochimica Acta* **141**, 145–159. https://doi.org/10.1016/j.gca.2014.05.050.

Weiss, Y., McNeill, J., Pearson, D. G., Nowell, G. M. & Ottley, C. J. (2015). Highly saline fluids from a subducting slab as the source for fluid-rich diamonds. *Nature* **524**, 339–342. https://doi.org/10.1038/nature14857.

Weiss, Y., Czas, J. & Navon, O. (2022). Fluid inclusions in fibrous diamonds. *Reviews in Mineralogy and Geochemistry* **88**, 475–532. https://doi.org/10.2138/rmg.2022.88.09.

Wilding, M. C. (1990) *A study of diamonds with syngenetic inclusions*. University of Edinburgh, Edinburgh, UK, p.281.

Windom, K. E. & Boettcher, A. L. (1980). Mantle metasomatism and the kimberlite-lamprophyre association: evidence from an eclogite nodule from Roberts victor mine, South Africa. *Journal of Geology* **88**, 705–712. https://doi.org/10.1086/628556.

Yasuda, A., Fujii, T., & Kurita, K. (1994). Melting phase relations of an anhydrous mid-ocean ridge basalt from 3 to 20 GPa: Implications for the behavior of subducted oceanic crust in the mantle. *Journal of Geophysical Research: Solid Earth*, **99**(B5), 9401–9414. https://doi.org/10.1029/93jb03205.

Journal of Petrology, 2025, **66**, egaf036
https://doi.org/10.1093/petrology/egaf036
Original Manuscript